

Cryo-EM structures of the Caspase activated protein XKR9 involved in apoptotic lipid scrambling

Monique S. Straub¹, Carolina Alvadia¹, Marta Sawicka¹ and Raimund Dutzler^{1*}

¹ Department of Biochemistry, University of Zurich, Switzerland

*For correspondence: dutzler@bioc.uzh.ch (RD)

Abstract

The exposure of the negatively charged lipid phosphatidylserine on the cell-surface, catalyzed by lipid scramblases, is an important signal for the clearance of apoptotic cells by macrophages. The protein XKR9 is a member of a conserved family that has been associated with apoptotic lipid scrambling. Here, we describe structures of full-length and caspase-treated XKR9 in complex with a synthetic nanobody determined by cryo-electron microscopy. The 43 kDa monomeric membrane protein contains eight membrane-spanning helices, two segments that are partly inserted into the lipid bilayer and is organized as two structurally related repeats. In the full-length protein, the C-terminus interacts with a hydrophobic site located at the intracellular side acting as an inhibitor of protein function. Cleavage by caspase-3 at a specific site releases 16 residues of the C-terminus thus making the binding site accessible to the cytoplasm. Collectively, the work has revealed the unknown architecture of the XKR family and has provided initial insight into its activation by caspases.

Introduction

The lipid distribution in the two leaflets of the plasma membrane of a eukaryotic cell is asymmetric with phosphatidylethanolamine (PE) and the anionic lipids phosphatidylserine (PS) and phosphoinositol (PI) located in the inner leaflet and phosphatidylcholine (PC) and sphingomyelin (SM), in the outer leaflet of the bilayer (Balasubramanian and Schroit, 2003; Bevers and Williamson, 2016; Kobayashi and Menon, 2018). This asymmetry is established and maintained by ATP-dependent active transport processes (Leventis and Grinstein, 2010; Sebastian et al., 2012). Although preserved under resting conditions, the controlled breakdown of the lipid asymmetry changes the properties of the membrane and is exploited in different processes ranging from signal transduction to membrane fusion (Nagata et al., 2016; Whitlock and Hartzell, 2016). Asymmetry breakdown is catalyzed by lipid channels termed scramblases, which catalyze the bidirectional diffusion of lipids with poor specificity by lowering the barrier for lipid flip-flop between the two leaflets of the membrane (Brunner et al., 2016; Nagata et al., 2020; Pomorski and Menon, 2006). The resulting equilibration causes the exposure of negatively charged PS to the outside, which serves as a receptor for proteins that initiate specific signaling cascades. In case of apoptosis, PS exposure serves as an eat-me signal for macrophages, leading to the engulfment and clearance of apoptotic cells (Segawa and Nagata, 2015). To prevent endogenous activity, which would be deleterious to cells, scramblases residing at the plasma membrane are tightly regulated. While incapable of catalyzing lipid transport under resting conditions, they become activated by specific stimuli which lead to conformational rearrangements of the protein (Nagata et al., 2020). Active scramblases are believed to function by a ‘credit card-like mechanism’, by offering suitable pathways for lipid headgroups to cross the hydrophobic membrane core whereas their apolar tails reside in the membrane (Pomorski and Menon, 2006).

Lipid scrambling is catalyzed by different proteins with the currently best characterized examples belonging to the TMEM16 and XKR families (Suzuki et al., 2013; Suzuki et al., 2010). TMEM16 scramblases are activated in response to the increase of the intracellular Ca^{2+} concentration. Their mechanism of activation and lipid transport are best understood for the two fungal homologues nhTMEM16 and afTMEM16 (Brunner et al., 2014; Falzone et al., 2019; Kalienkova et al., 2019; Kalienkova et al., 2021). These proteins contain polar membrane-spanning furrows of appropriate size, which are blocked in the absence of Ca^{2+} but become exposed to the membrane upon Ca^{2+} binding to offer suitable pathways for polar headgroups across the membrane, as predicted by the ‘credit card mechanism’. The fungal TMEM16 proteins were also found to disturb the organization of lipids in their vicinity, likely by destabilizing the bilayer and thus further decreasing the barrier for lipid flip-flop (Falzone et al., 2019; Kalienkova et al., 2019).

Although scramblases of the TMEM16 family have been associated with diverse processes such as blood coagulation and cell-fusion, they are not the long sought-after scramblases that are responsible for the exposure of PS during apoptosis. The molecular identity of an apoptotic scramblase was identified eight years ago when the human protein XKR8 and its *C. elegans* homologue Ced-8 were assigned as the scramblases that are responsible for PS exposure in apoptotic cells (Chen et al., 2013; Suzuki et al., 2013). Both are part of the evolutionarily conserved XKR family of proteins related to the founding member XK1, a molecule with unknown function, which was identified to be associated with the blood-group specific factor Kell (Calenda et al., 2006; Stanfield and Horvitz, 2000). In humans, the family contains nine members, three of which, namely the proteins XKR4, 8 and 9, were found to activate scrambling under apoptotic conditions (Suzuki et al., 2014). The primary activating step is the cleavage of a C-terminal peptide by the apoptotic peptidase Caspase-3 at a specific site that is found in all three proteins (Suzuki et al., 2013; Suzuki et al., 2014). Besides the irreversible

action of caspases, XKR8 was also shown to be activated by phosphorylation (Sakuragi et al., 2019).

A more recent study has revealed the association of XKR8 with accessory proteins such as basigin or its paralogue neuropilin (Suzuki et al., 2016). Both class 1 membrane proteins, containing extracellular IG-domains, facilitate the targeting of XKR8 to the plasma membrane. Based on the altered migration behavior on blue-native gel electrophoresis, the same study also claimed a dimerization of XKR8-basigin complexes upon caspase-3 activation as an essential step underlying activation (Suzuki et al., 2016). A similar dimerization was recently postulated for the scramblase XKR4 (Maruoka et al., 2021).

Whereas the central role of certain XKR proteins in apoptotic scrambling and their activation by caspase-3 has been conclusively demonstrated, their molecular architecture and the question whether or how the proteins on their own would catalyze lipid transport has remained elusive. To address these questions, we have here studied the protein XKR9 from *Rattus norvegicus* and determined its structure in its full-length and caspase-cleaved form by cryo-electron microscopy (cryo-EM). Our results reveal the novel architecture of a eukaryotic membrane protein family involved in apoptotic scrambling and provide insight into their activation mechanism.

Results

Biochemical characterization of XKR9

In our study, we have selected the XKR9 orthologue from *Rattus norvegicus* (rXKR9) due to its promising biochemical properties. The protein is 373 amino acids long and shares 76% of identical residues with its human orthologue. Following its expression in suspension culture of HEK293S GnTI⁻ cells, purification in the detergent lauryl maltose neopentyl glycol (LMNG) and removal of the N-terminal tag used for affinity purification, we found rXKR9 to elute as

monodisperse peak on gel-filtration with an elution volume corresponding to a monomer (Figure 1A), which was subsequently quantified by multi angle light scattering (Figure 1—figure supplement 1A). The protein contains a predicted caspase cleavage site, which would remove 16 amino acids from the C-terminus resulting in the activation of scrambling in cells. We have investigated protein digestion after incubation with caspase-3 in detergent solution and found complete cleavage of the C-terminus resulting in the predicted reduction of the molecular weight as confirmed by mass spectrometry. As full-length rXKR9, the truncated protein elutes as a monomer and we did not find strong evidence of dimerization in detergent solution (Figure 1B), which was independently suggested for an XKR8-basigin complex (Suzuki et al., 2016) and for XKR4 upon caspase activation (Maruoka et al., 2021). To probe whether purified rXKR9 on its own would facilitate lipid scrambling, we have reconstituted the protein into liposomes. Proper formation of proteoliposomes was assayed by the re-extraction of the reconstituted protein in mild detergents and its analysis by size exclusion chromatography (Figure 1—figure supplement 1B). We subsequently investigated the flipping of lipids between the two leaflets of the bilayer by using an assay that was previously established for the characterization of opsin and scramblases of the TMEM16 family (Brunner and Schenck, 2019; Falzone and Accardi, 2020; Ploier and Menon, 2016). The applied assay investigates the quenching of a fluorescent NBD group attached to one of the tails of a lipid that was added to the liposomes as minor component. The reduction of fluorescence proceeded by addition of the membrane-impermeable reagent dithionite to the outside, which bleaches NBD-containing lipids located on the outer leaflet of the bilayer. In our assays, we investigated the scrambling activity in proteoliposomes containing either full-length rXKR9, a truncated form of the protein where the C-terminus was cleaved-off before reconstitution, or proteoliposomes of full-length rXKR9 where the accessible C-terminus of proteins in inside-out orientation was removed upon addition of caspase-3 to the medium. In latter case, reducing conditions were required for the protease to be active, which was achieved by supplementation of the buffer with 1mM of TCEP,

which did neither reduce the labeled lipids nor interfere with liposome integrity. Whereas in both cases, cleavage was detected on SDS-PAGE (Figure 1C), the assay used to investigate the integrity of the reconstituted protein indicated that removal of the C-terminus might have compromised the stability of rXKR9, which is particularly pronounced for protein that was incubated with caspase-3 prior to reconstitution. After re-extraction of the digested protein from proteoliposomes, we found for cleaved protein a decreasing peak height at elution volumes corresponding to monomers and pronounced peaks eluting at the void volume of the column (Figure 1—figure supplement 1B). In our liposome-based assays, we did not find any evidence of scrambling activity irrespective of the cleavage of the C-terminus (Figure 1D, Figure 1—figure supplement 1C), thus suggesting that the protein does not promote lipid scrambling under the applied conditions, which might be the consequence of the lack of an essential factor required for the protein to be active.

Since the human homologue hXKR8 was shown to form a complex with the accessory protein basigin (Suzuki et al., 2016), we wondered whether the latter might be a mandatory factor for scrambling activity of rXKR9 and thus engaged in biochemical studies investigating the co-expression of either protein with their corresponding species-specific basigin orthologs. Whereas in case of hXKR8 we find robust complex formation with basigin, which is also manifested in a low-resolution cryo-EM reconstruction (Figure 1E, F), we do not find evidence for the formation of a similar complex with rXKR9 (Figure 1G), thus refuting the assumption that basigin might be the essential partner that would convert rXKR9 into an active scramblase.

Structure determination of XKR9-sybody complexes

Although rXKR9 did not show any scrambling activity *in vitro*, its high similarity to hXKR8 (with both proteins sharing 29% of identical and 53% of homologous residues) and its susceptibility to caspase-3 makes it an attractive target to elucidate the unknown architecture of

the XKR family and the molecular consequences of its proteolytic activation. As a monomeric protein containing 373 residues only, rXKR9 is on the small side for structural studies by cryo-EM and we thus attempted to increase its size by forming complexes with suitable binding proteins. To this end, we engaged in the selection of nanobodies from synthetic libraries (termed sybodies) targeting purified rXKR9 by a combination of ribosome- and phage-display (Zimmermann et al., 2018; Zimmermann et al., 2020). Our attempts allowed us to identify several sybodies. From the selected set of binders, we chose the sybody Sb1^{XKR9} to generate complexes with full-length and cleaved rXKR9 due to its ability to form stable and monodisperse heterodimeric 1:1 complexes (Figure 1—figure supplement 3).

Following sample preparation, we collected large cryo-EM datasets of both complexes. The resulting maps, which extend to 3.66 Å for full-length and 4.3 Å for the cleaved protein, were of high quality and allowed in each case the interpretation with an atomic model (Figure 2, Figure 2—figure supplements 1-3, Table 1). The structure was initially built into the map of the full-length protein (Figure 2A). Although, due the novelty of the protein fold, model building was challenging, the high quality of the map and the distribution of sidechain density of different volume has ultimately allowed the unambiguous interpretation of residues 1-66, 81-105, 119-344 and 365-373 of rXKR9 encompassing all structured parts of the protein. In case of Sb1^{XKR9}, the density of the CDR regions in contact with the protein are of high quality and revealed the interaction with its epitope, whereas the more peripheral residues are of lower resolution and were thus interpreted with a model that is based on a high-resolution structure of the constant region (Figure 2—figure supplement 3B, D). The structure of the cleaved rXKR9-Sb1^{XKR9} complex was subsequently built using the full-length complex as template, which was comparably straightforward, since the bulk of the protein retained a similar conformation, and the density that was ascribed to the C-terminus in the data of the full-length protein was absent (Figure 2B).

The structures of the XKR9-sybody complexes are shown in Figure 3. Viewed perpendicular to the membrane, the entire complex is about 80 Å high, and measures 40 x 35 Å within the membrane plane. On the extracellular side, rXKR9 extends barely beyond the membrane boundary and does not contain any glycosylation sites. Sb1^{XKR9} binds to this region burying 1466 Å² of the combined molecular surface. Sybody contacts are mainly formed by the long CDR3, which wraps around the loop connecting TM3-4 and wedges into the cleft towards the adjacent TM7-TM8 loop (Figure 3—figure supplement 1).

XKR9 architecture

rXKR9 comprises eight membrane-spanning helices (TM1-8), which are connected by short loops on the extracellular and longer loops on the intracellular side (Figure 4A-C). Two particularly long intracellular regions harbor α-helices (IH1 and IH2) that are partly inserted in the membrane, other segments are disordered and protrude into the cytoplasm. Although the number of transmembrane helices concurs with predictions by hydropathy analysis (Krogh et al., 2001), there is some discrepancy with respect to their location. Whereas seven of the helices were correctly predicted, due to its hydrophilic character, the highly conserved TM3 was not assigned as membrane-spanning segment. Conversely, the sixth predicted segment forms the hydrophobic helix IH2 that only spans the inner membrane leaflet and is connected to TM7 by a re-entrant loop (Figure 4—figure supplement 1).

The rXKR9 structure consists of two consecutive domains (the N-terminal domain ND and C-terminal domain CD) with similar general organization containing four membrane-spanning helices each (Figure 4B, D). The first two helices of each repeat (*i.e.* TM1-TM2 and TM5-TM6) interact at the extracellular side but are splayed open towards the inside to make space for the respective helical regions IH1 and IH2 that are contained within loops and inserted into the inner leaflet of the membrane (Figure 4C). The second pair of helices in each domain run

parallel and make contacts throughout the membrane. IH1 is located at the periphery of the protein and engages in interactions with TM3. IH2, in contrast, is wedged between both domains to fill the intracellular part of a cavity that is formed at their interface (Figure 4C, D). The long hydrophilic transmembrane helix TM3 is kinked in the center of the membrane at a conserved PQL motive, which causes a bending away from the membrane normal on its intracellular part to maximize interactions with IH1 (Figure 4C).

Features of potential functional relevance

Previous studies on the phospholipid scramblase nhTMEM16 have identified a membrane-spanning furrow as structural hallmark of the protein (Brunner et al., 2014). This polar furrow is of appropriate size to harbor a phospholipid headgroup and might thus provide a favorable environment for the translocation of lipid headgroups. Consequently, we analyzed the rXKR9 structure for analogous features. Two furrow-like structures of appropriate size to harbor a lipid are found at the interface between the two domains of rXKR9 on both sides of the molecule and an additional structural feature of similar shape is contained within the C-terminal domain (Figure 5A). On one side of the domain interface, a cavity formed by the helices TM2, 3, 5 and 6 is on its intracellular part filled with the helix IH2 (Figure 5A, B). Its appropriate dimensions are underlined by a bound lipid molecule observed in our structure (Figure 5B). On the opposite side of the molecule, a similar cavity is formed by TM3, 4, 5, and 8, which is filled towards the intracellular side by the tilted α -helix TM5 (Figure 5A, C). On its intracellular side, outside of the hydrophobic membrane core, this region contains a cluster of basic amino acids, which contribute to a patch of strong positive potential and might interact with the headgroups of negatively charged lipids (Figure 5—figure supplement 1). The third cavity contained within the C-terminal domain is formed by helices TM5, 6, and 7 (Figure 5A, D). In all three cases,

the generally hydrophobic character of the described cavities renders their suitability as a lipid translocation path ambiguous (Figure 5A-D).

A second hallmark of a lipid scramblase relates to polar residues that are embedded within the membrane-inserted part of the protein, which in its active conformation, would be exposed to the bilayer to lower the energy barrier for lipid flip-flop (Bethel and Grabe, 2016; Brunner et al., 2014; Jiang et al., 2017; Lee et al., 2018; Stansfeld et al., 2015). Although the transmembrane helices of rXKR9 contain several polar and charged residues, which have precluded the assignment of TM3 as membrane-spanning region during hydropathy analysis (Figure 4A, Figure 4—figure supplement 1), the observed protein conformation buries these residues between the tightly packed transmembrane segments. Due to the long-range nature of coulombic interactions and the low dielectrics of the bilayer, these residues might still influence the electrostatics on the surface of the protein and thus its ability to interact with polar compounds (Figure 5—figure supplement 1). A region with high density of acidic residues is positioned between interacting helices of the N-terminal domain (Figure 5E, F). These residues, which are predominantly located on TM1 and 3, are strongly conserved throughout the family and thus appear to be a characteristic feature of XKR proteins (Figure 5F, G). Occluded within the core of the N-terminal domain, the vicinity of several acidic residues distantly resembles a divalent cation binding site, although the structure does not provide evidence of bound cations (Figure 5F). Conversely, a cluster of polar and basic residues is located at the C-terminal domain and render the electrostatics positive (Figure 5H-I). In contrast to the N-terminal domain, these residues are less conserved (Figure 5J) and one buried arginine (Arg 294) appears to interact with the C-terminus of the partly inserted helix IH2, suggesting that it would serve a role in the stabilization of the structure (Figure 5H).

In summary, while the presence of charged residues located within the membrane domain, some of which are strongly conserved, emphasize their importance for protein stability, their role for

lipid movement, and the question whether some of them would change their exposure during activation is currently still unclear.

Activation

Activation of apoptotic scramblases proceeds after cleavage of a C-terminal peptide by caspase-3 at a specific recognition site (Figure 4A). In case of rXKR9, part of the cleavable peptide, which is only 16 residues long, binds to an intracellular site that is located in a pocket at the interface between the two domains formed by residues of TM3-5, 8, IH2 and the connecting loop regions (Figure 6A, B). In the structure of full-length rXKR9, part of the inhibitory peptide is well-defined, whereas the connecting loop containing the cleavage site appears unstructured (Figure 2A, Figure 2—figure supplement 4). Features in the density suggest the binding of eight residues at the very C-terminus of the protein that fold into a single turn of an α -helix followed by an extended region to form complementary interactions with the protein burying 1698 Å² of the combined molecular surface (Figures 3B and 6A). In our model, the C-terminus fills the binding pocket to either stabilize the protein in its inactive form or, alternatively, shield the residues lining the pocket from other interactions. The binding is predominantly hydrophobic at its core but involves coulombic interactions at the periphery (Figure 6C). An isoleucine (Ile 367), a phenylalanine (Phe 370) and a leucine (Leu 371) of the C-terminus are buried in a hydrophobic pocket of the protein that is lined by aliphatic and aromatic residues (Figure 6D). In the data of the cleaved rXKR9, the density of the C-terminus is absent, exposing the hydrophobic cleft to the cytoplasm (Figure 2). Apart from smaller changes in the intracellular loop regions, the truncated protein has not changed its conformation, which is illustrated in the low RMSD of 0.72 Å between the two structures (Figure 6B). However, at this stage we do not want to exclude the possibility of larger conformational changes during activation as the observed conformation might be either be stabilized by the bound sybody or the absence of an

endogenous factor that has also prohibited lipid scrambling in reconstituted samples (Figure 1C).

Discussion

By determining the structure of full-length rXKR9 and its caspase-cleaved form by cryo-EM, our study has revealed the architecture of the XKR family and provided a first glimpse on its activation. With a size of only 43 kDa and not containing pronounced structural features outside of the membrane, rXKR9 on its own is too small for cryo-EM analysis. However, the addition of a sybody increasing the complex size to 60 kDa was sufficient to obtain high quality data and thus could provide a suitable general strategy for the structure determination of small and asymmetric membrane proteins. The rXKR9 structures show a novel protein fold, consisting of two structurally related repeats of four transmembrane helices each, that is presumably shared by the entire family irrespective of the function of its members, which is in many cases still elusive.

Three members of the XKR family, namely the proteins XKR8, 9 and 4, were previously identified as essential constituents of apoptotic lipid scramblases, which are activated by proteolysis (Suzuki et al., 2014). Caspases directly act on the protein by targeting a single cleavage site located after the last transmembrane helix TM8 (Figure 4A). Our structures illustrate the consequence of this cleavage where the C-terminus, which binds to a hydrophobic pocket facing the cytoplasm in the full-length protein, is released to free the access to this site (Figures 4B, D and 6). The 16-residue-long peptide thus acts as inhibitor of protein function, whose dissociation from its binding site is a requirement for activation. This could either proceed by lowering its local concentration following proteolysis or by covalent modifications of the peptide as recently suggested for XKR8, which is also activated by phosphorylation of specific positions of the C-terminus (Sakuragi et al., 2019).

Although in our structure of the cleaved rXKR9, we do not observe any larger rearrangements of the protein as a consequence of proteolysis (Figure 6B), such conformational changes could be prevented by the bound sybody or the lack of accessory factors, which might lock the protein in its observed conformation. Although previous experimental data suggested that XKR proteins themselves form the catalytic unit promoting scrambling activity (Suzuki et al., 2013; Suzuki et al., 2014), our attempts to observe such activity for rXKR9 *in vitro* after purification and reconstitution into liposomes did not provide evidence for lipid flip-flop (Figure 1D). This does not exclude that rXKR9 would itself act as a scramblase, but it suggests that there might be additional components required for its activity. In case of its paralog XKR8, this could be the interaction with the β -subunit basigin (Figure 1E, F) and the proposed dimerization of the complex upon activation (Suzuki et al., 2016). Pairing in response to caspase cleavage was recently also reported for the protein XKR4, which additionally requires the binding of an endogenous peptide for activation (Maruoka et al., 2021). For rXKR9, we did neither observe an interaction with basigin, nor did we find any indication for the change of the oligomeric state following caspase cleavage (Figure 1B, D), leaving the possibility that the protein might require an unknown subunit for activation and lipid transport.

Previous studies on fungal homologues of the TMEM16 family have defined features that underlie their function as lipid scramblases. These include a protein architecture that distorts the membrane and the presence of a hydrophilic membrane-spanning furrow that is hidden in the closed conformation and that becomes exposed in the activated conformation of the protein (Bethel and Grabe, 2016; Brunner et al., 2014; Falzone et al., 2019; Kalienkova et al., 2019). Both factors appear sufficient to lower the energetic barrier for lipid flip-flop, which might proceed in the immediate vicinity of the polar furrow and even at some distance from the protein (Malvezzi et al., 2018). No such obvious features for scramblase function were found in the rXKR9 structures (Figure 2—figure supplement 3A, C). The micelle surrounding the protein does not show clear evidence for distortion, which in fungal TMEM16 scramblases was already

manifested in structures determined in detergents (Kalienkova et al., 2019). Moreover, appropriate cavities located at the surface of the protein, which contain residual densities of bound lipids, are generally hydrophobic and thus do not offer obvious interactions with the lipid headgroups on their way across the membrane (Figures 2 and 5A-D). Polar amino acids on the surface of rXKR9 are generally found in the headgroup region, including a cluster of positively charged residues located at the intracellular side of one cavity, which might facilitate the interaction with negatively charged lipids (Figure 5—figure supplement 1C). A remarkable feature of rXKR9 concerns a cluster of acidic residues buried in the protein, which is strongly conserved within family members that were assigned as lipid scramblases, with TM3 being unusually hydrophilic for a transmembrane helix (Figure 5E-G). The role of these residues for protein function is currently unknown, and it is conceivable that they might contribute to lipid scrambling in an active state of the protein, which is likely not displayed in any of our structures. Due to the low dielectric environment of the membrane, charged residues might influence the interaction with polar lipid headgroups even in case they would remain buried after activation (Figure 5—figure supplement 1). In light of the lack of structural evidence for its scramblase function, it is noteworthy that opsins were demonstrated to function as lipid scramblases without containing obvious structural features (Menon et al., 2011; Morra et al., 2018) and that the hallmarks described for the fungal scramblases nhTMEM16 (Brunner et al., 2014), afTMEM16 (Falzone et al., 2019) or TMEM16K (Bushell et al., 2019) are not displayed in any of the current structures of TMEM16F, whose function as lipid scramblase has been demonstrated *in vivo* and *in vitro* (Alvadia et al., 2019; Suzuki et al., 2010).

In summary, our study has defined the architecture of a protein that forms an essential part of the machinery leading to the exposure of PS during programmed cell death, which is an essential step leading to the clearance of apoptotic cells (Segawa and Nagata, 2015). By defining the interaction of the C-terminus, which is removed upon proteolysis, it has also provided initial insight into the activation of family members by caspases. However, as we did

not observe activity of rXKR9 upon reconstitution and its structure structures do not provide immediate evidence for a potential scrambling mechanism, we do currently foresee different scenarios for activation and lipid transport (Figure 7). These include a conformational change that would expose polar patches that are buried in the inactive protein to facilitate lipid flip-flop. In the observed caspase-cleaved structure, these might have been prevented by the bound sybody or the lack of a suitable membrane environment. Activation might also require dimerization of the protein as suggested for XKR8 and XKR4 (Maruoka et al., 2021; Suzuki et al., 2016). Alternatively, the protein could require an extrinsic interaction partner that might contribute part or all of the site responsible for lipid flip-flop. With the accessory protein basigin, such interaction partner has already been identified for XKR8 (Suzuki et al., 2016). Finally, the dissociation of the C-terminus following caspase cleavage might open up a site for the interaction with an accessory factor, which was described in a recent study of XKR4 (Maruoka et al., 2021). These mechanisms could also work in concert to promote the activation of an apoptotic scramblase. Collectively, our work provides a foundation for future experiments that will have to clarify whether and how the members of this important protein family catalyze lipid translocation between membrane leaflets and identify interaction partners that may play a critical role in their function.

Material and Methods

Key resources table

Reagent type	Designation	Source or reference	Identifiers	Additional information
Cell line (human)	HEK239T	ATCC	CRL-3216	
Cell line (human)	HEK293S GnTI	ATCC	CRL-3022	
Chemical compound, drug	18:1 06:0 NBD-PE	Avanti Polar Lipids	810155C	
Chemical compound, drug	18:1 06:0 NBD-PS	Avanti Polar Lipids	810194C	
Chemical compound, drug	1-palmitoyl-2-oleoyl-sn-glycero-3-phospho-(1'-rac-glycerol) (18:1 06:0 POPG)	Avanti Polar Lipids	840457C	

Chemical compound, drug	1-palmitoyl-2-oleoyl-sn-glycero-3-phosphocholine (18:1 06:0 POPC)	Avanti Polar Lipids	850457C	
Chemical compound, drug	1-palmitoyl-2-oleoyl-sn-glycero-3-phosphoethanolamine (18:1 06:0 POPE)	Avanti Polar Lipids	850757C	
Chemical compound, drug	Benzamidine	Sigma	B6506	
Chemical compound, drug	Biotin	Sigma	B4501	
Chemical compound, drug	Calcium nitrate tetrahydrate	Sigma	C4955	
Chemical compound, drug	CHAPS	Sigma	C3023	
Chemical compound, drug	Chloramphenicol	Sigma	C1919	
Chemical compound, drug	Chloroform	Fluka	25690	
Chemical compound, drug	Cholesterol	Sigma	C3045	
Chemical compound, drug	cOmplete, EDTA-free Protease Inhibitor Cocktail	Roche	5056489001	
Chemical compound, drug	D-Desthiobiotin	Sigma	D1411	
Chemical compound, drug	DDM	Anatrace	D310S	
Chemical compound, drug	Diethyl ether	Sigma	296082	
Chemical compound, drug	Digitonin High Purity	Merck Millipore	300410	
Chemical compound, drug	DNase I	AppliChem	A3778	
Chemical compound, drug	DTT	ThermoFisher Scientific	R0861	
Chemical compound, drug	Dulbecco's modified Eagle's medium - high glucose	Gibco, ThermoFisher Scientific	41966029	
Chemical compound, drug	Ethyleneglycol - bis (2 - aminoethylether) - N,N,N',N' - tetraaceticacid	Sigma	E3889	
Chemical compound, drug	Fetal Bovine Serum	Sigma	F7524	
Chemical compound, drug	GDN	Anatrace	GDN101	
Chemical compound, drug	glycerol 99%	Sigma	G7757	
Chemical compound, drug	HCl	Merck Millipore	1.00319.1000	
Chemical compound, drug	HEPES	Sigma	H3375	
Chemical compound, drug	HyClone HyCell TransFx-H medium	Cytiva	SH30939.02	
Chemical compound, drug	Imidazole	Roth	X998.4	
Chemical compound, drug	Kolliphor P188	Sigma	K4894	
Chemical compound, drug	L-(+)-arabinose	Sigma	A3256	
Chemical compound, drug	Lauryl-maltose-neopentyl glycol (LMNG)	Anatrace	NG310	
Chemical compound, drug	Leupeptin	AppliChem	A2183	
Chemical compound, drug	L-glutamine	Sigma	G7513	
Chemical compound, drug	Penicillin-streptomycin	Sigma	P0781	
Chemical compound, drug	Pepstatin	AppliChem	A2205	
Chemical compound, drug	Phosphate buffered saline	Sigma	D8537	
Chemical compound, drug	PMSF	Sigma	P7626	
Chemical compound, drug	Polyethyleneimine MAX 40 kDa	PolySciences Inc.	24765-1	
Chemical compound, drug	Potassium chloride	Sigma	746346	

Chemical compound, drug	Sodium chloride	Sigma	71380	
Chemical compound, drug	Sodium dithionite (Sodium hydrosulfite)	Sigma	157953	
Chemical compound, drug	Soybean Polar Lipids	Avanti Polar Lipids	541602C	
Chemical compound, drug	TCEP	Hampton	HR2-651	
Chemical compound, drug	Terrific broth	Sigma	T9179	
Chemical compound, drug	Tetracycline hydrochloride	Sigma	T7660	
Chemical compound, drug	Tris	AppliChem	A1379	
Chemical compound, drug	Valproic acid	Sigma	P4543	
Commercial assay or kit	4–20% Mini-PROTEAN® TGX™ Precast Protein Gels, 15-well, 15 µl	BioRad Laboratories	4561096DC	
Commercial assay or kit	Amicon Ultra-4 Centrifugal Filters Ultracel 10K, 4 ml	Merck Millipore	UFC801096	
Commercial assay or kit	Amicon Ultra-4 Centrifugal Filters Ultracel 50K, 4 ml	Merck Millipore	UFC805096	
Commercial assay or kit	Amicon Ultra-4 Centrifugal Filters Ultracel 100K, 4 ml	Merck Millipore	UFC810024	
Commercial assay or kit	Biobeads SM-2 adsorbents	BioRad Laboratories	152-3920	
Commercial assay or kit	EZ-link™ NHS-PEG4-biotin	ThermoFisher Scientific	A39259	
Commercial assay or kit	MiniExtruder	Avanti Polar Lipids	610023	
Commercial assay or kit	Ni-NTA resin	ABT Agarose Bead Technologies	6BCL-NTANi-X	
Commercial assay or kit	Nunc 384-well plate MaxiSorp	ThermoFisher Scientific	460372	
Commercial assay or kit	PC membrane 0.2µm	Avanti Polar Lipids	610006	
Commercial assay or kit	PD-10 desalting column	Sigma	GE17-0851-01	
Commercial assay or kit	Pierce Streptavidin Plus UltraLink Resin	ThermoFisher Scientific	53117	
Commercial assay or kit	QuantiFoil R1.2/1.3 Au 200 mesh	Electron Microscopy Sciences	Q2100AR1.3	
Commercial assay or kit	Silver Stain Plus™	BioRad Laboratories	161-0449	
Commercial assay or kit	SRT-10C SEC 100	Sepax Technologies	239100-10030	
Commercial assay or kit	Strep-Tactin® Superflow® high capacity 50% suspension	IBA LifeSciences	2-1208-010	
Commercial assay or kit	Superdex 200 10/300 GL	Cytiva	17517501	
Commercial assay or kit	Superdex 200 Increase 3.2/300	Cytiva	28990946	
Commercial assay or kit	Superdex 200 Increase 5/150 GL	Cytiva	28990945	
Commercial assay or kit	Superdex 75 10/300 GL	Cytiva	17517401	
Commercial assay or kit	Superose 6 10/300 GL	Cytiva	17517201	
Commercial assay or kit	Superose 6 Increase 5/150	Cytiva	29091597	
Commercial assay or kit	Ultrafree MC GV 0.22µm centrifugal filter	Merck Millipore	UFC30GVNB	
Commercial assay or kit	Ultrafree - MC -HV, DURAPORE PVDF 0.1µm	Merck Millipore	UFC30VV00	
Other	BioQuantum Energy Filter	Gatan	NA	
Other	Fluoromax spectrometer	Horiba	NA	
Other	HPL6	Maximator	NA	
Other	K2 Summit Direct Detector	Gatan	NA	
Other	K3 Summit Direct Detector	Gatan	NA	
Other	qPCR machine Mx3005p	Agilent	NA	
Other	Sybody library	Generous gift from the Seeger laboratory	NA	
Other	Tecna G ² Polara	ThermoFisher Scientific	NA	

Other	Titan Krios G3i	ThermoFisher Scientific	NA	
Other	UT-rEX Refractometer	Wyatt Technology	NA	
Other	Viber Fusion FX7 imaging system	Witec	NA	
Other	Vitrobot Mark IV	ThermoFisher Scientific	NA	
Other	μDAWN MALS Detector	Wyatt Technology	NA	
recombinant DNA	human Basigin open reading frame	GenScript	HUMBSG	
recombinant DNA	human Xkr8 open reading frame	GenScript	NM 018053	
recombinant DNA	Mammalian expression vector with C-terminal 3C cleavage site, GFP-tag and myc-tag	Dutzler laboratory	NA	
recombinant DNA	Mammalian expression vector with N-terminal streptavidin binding peptide, myc-tag and 3C cleavage site	Dutzler laboratory	NA	
recombinant DNA	Mammalian expression vector with N-terminal streptavidin binding peptide, myc-tag, Venus-tag and 3C cleavage site	Dutzler laboratory	NA	
Recombinant DNA	Mouse mTMEM16F open reading frame	Dharmacon - Horizon Discovery	GenBank#BC060732	
recombinant DNA	pSb init	Generous gift from the Seeger laboratory	Addgene #110100	
recombinant DNA	rat basigin open reading frame	GenScript	NM 012783	
recombinant DNA	rat XKR9 open reading frame	GenScript	NM 001012229	
recombinant protein	HRV 3C protease	Expressed (pET_3C) and purified in Dutzler laboratory	NA	
recombinant protein	Human Caspase-3, recombinant	BioVision	1083	
recombinant protein	Streptavidin	Expressed and purified in Dutzler laboratory	NA	
Software, algorithm	3DFSC	Tan et al., 2017	https://3dfsc.salk.edu/	
Software, algorithm	ASTRA7.2	Wyatt Technology	https://www.wyatt.com/products/software/astra.html	
Software, algorithm	Chimera v.1.15	Pettersen et al., 2004	https://www.cgl.ucsf.edu/chimera/	
Software, algorithm	ChimeraX v.1.1.1	Pettersen et al., 2021	https://www.rbvi.ucsf.edu/chimerax/	
Software, algorithm	Coot v.0.9.4	Emsley et al., 2010	https://www2.mrc-lmb.cam.ac.uk/personal/pemsley/coot/	
Software, algorithm	cryoSPARC v.3.0.1/v.3.2.0	Structura Biotechnology Inc.	https://cryosparc.com/	
Software, algorithm	DINO		http://www.dino3d.org	
Software, algorithm	EPU2.9	ThermoFisher Scientific	NA	
Software, algorithm	Codon optimization tool	Integrated DNA technologies	https://eu.idtdna.com/pages/tools/codon-optimization-tool	
Software, algorithm	Phenix	Liebschner et al., 2019	https://www.phenix-online.org/	
Software, algorithm	RELION 3.0.7	Zivanov et al., 2018	https://www3.mrc-lmb.cam.ac.uk/relion/	
Software, algorithm	SerialEM3.7	Mastronarde, 2005	https://bio3d.colorado.edu/SerialEM/	
Software, algorithm	WEBMAXC calculator	Bers et al., 2010	https://somapp.ucdmc.ucdavis.edu/pharmacology/bers/maxchelator/webmaxc/webmaxcS.htm	
Strain	E. coli MC1061	ThermoFisher Scientific	C66303	

367

368

369 **Construct preparation**

The genes were codon-optimized for mammalian expression (IDT codon optimization tool) and synthesized by GenScript. The genes were subsequently cloned into pcDNA 3.1 (pcDx) expression vectors by FX-cloning (Geertsma and Dutzler, 2011). rXKR9 and hXKR8 were cloned into two different pcDx vectors, one with a N-terminal streptavidin binding peptide (SBP), myc-tag, and human rhinovirus (HRV) 3C cleavage site (pcDxNSM3), the other one harboring an additional Venus YFP tag in front of the 3C cleavage site (pcDxNSMV3). For co-purification, rat and human basigin were cloned into a pcDx vector containing a 3C cleavage site, GFP, and a myc tag (pcDxC3GM).

The sybody sequences were cloned into the FX-compatible, chloramphenicol-resistant and arabinose-inducible pSb_init (Zimmermann et al., 2020), containing an N-terminal pelB leader sequence and a C-terminal hexa-histidine tag.

Protein expression and purification

rXKR9 was expressed in HEK293S GnTI⁻ cells adapted to suspension culture, grown in HyCell HyClone Trans Fx-H media supplemented with 1% FBS, 4 mM L-glutamine, 100 U/ml penicillin-streptomycin, and 1.5 g/l Kolliphor-184 at 37°C and 5% CO₂. For transient transfection, purified plasmid DNA was mixed with PEI MAX in a 1:2.5 ratio, diluted in non-supplemented DMEM medium to 0.01 mg DNA per ml, and incubated for 15 minutes at room temperature prior to addition to the cells. 3.5 mM valproic acid was added immediately after transfection. Cells were harvested 48 h post-transfection, washed in PBS, and pellets frozen in liquid N₂ and stored at -80°C until further use.

Frozen pellets were thawed on ice, re-suspended in lysis buffer (25 ml lysis buffer per 1 l of suspension culture), containing 25 mM HEPES pH7.5, 200 mM NaCl, 1% LMNG for rXKR9 and 2% GDN for hXKR8-hBSG, and protease inhibitors (0.1 μM PMSF, 10 μM leupeptin, 1 mM benzamidine, 1 μM pepstatin), and solubilized at 4 °C for 2 h, while gently mixing. The

solubilized protein was collected by ultracentrifugation at 85'000 g for 30 minutes at 4 °C and incubated with Streptactin superflow resin (1 ml 50% slurry for 1 l of suspension cell culture) for 2.5 h at 4°C under gentle agitation. The resin was washed with 50 column volumes (CV) of size exclusion chromatography (SEC) buffer (25 mM HEPES pH7.5, 200 mM NaCl, 0.01% LMNG or 0.03% GDN). The protein was eluted with 5 CV SEC buffer, supplemented with 10 mM desthiobiotin and incubated at 1:1 (wt/wt) ratio with HRV 3C protease for 45 minutes at 4 °C. The cleaved protein was concentrated using a 50 kDa cut-off concentrator for rXKR9 and a 100 kDa cut-off concentrator for hXKR8-hBSG at 500g in five-minute intervals at 4°C. The concentrated protein was filtered through a 0.22 µm filter and injected onto a Superdex 200 10/300 GL column, equilibrated in SEC buffer. Peak fractions were collected and concentrated as described above.

The sybody Sb1^{XKR9} was transformed into *E. coli* MC1061. Bacteria were grown in 1.2 l Terrific Broth media supplemented with 25 µg/ml chloramphenicol at 37°C. At OD₆₀₀ = 0.5, the temperature was decreased to 22 °C for 1.5 h and expression was induced with 0.02% L-arabinose for 16-18 hours. Bacterial cultures were harvested at 4'000 g for 20 minutes at 4 °C and pellets were frozen in liquid N₂ and stored at -80 °C. Frozen pellets were thawed on ice, re-suspended in lysis buffer TBS (36.5 mM Tris-HCl pH 7.4, 150 mM NaCl) supplemented with PMSF and DNase I at 100 ml per 1 l of culture. Cells were lysed using a high pressure lyser (HPL6) at 1-1.5 kbar and the lysate was centrifuged at 8'000g for 30 minutes at 4°C. Clarified lysate was supplemented with 30 mM Imidazole and incubated with 4 ml 50% Ni-NTA slurry per 1 l of culture for 2 h at 4°C under gentle agitation. Beads were washed with 25 CV TBS + 50 mM Imidazole and protein was eluted with 5 CV TBS with 300 mM Imidazole. The elution was concentrated with a 10 kDa cut-off concentrator at 3000 g in five-minute intervals, filtered through a 0.22 µm filter, and polished on a Superdex 75 10/300 GL column in TBS. Protein containing fractions were concentrated to 500 µM, frozen in liquid N₂, and stored at -80 °C.

420
421
422
423
424
425
426
427
428
429
430
431
432
433
434
435
436
437
438
439
440
441
442
443
444

Caspase-3 cleavage

One unit of recombinant human caspase-3 cleaves 1 nmol of its synthetic substrate at 37 °C in one hour. In case of rXKR9, the cleavage was performed at 4 °C overnight, using two units of caspase-3 per 1 nmol of purified rXKR9. To ensure caspase-3 activity, 10 mM DTT was supplemented. Caspase-3 cleaved protein was analyzed by ESI-MS by FGCZ at University of Zurich to confirm successful cleavage. Briefly, protein was precipitated with 30% aqueous solution of TCA. The pellet was washed two times in cold acetonitrile, before being dissolved in HIFP and diluted 1:1 with MeOH:2PrOH:0.2%FA (30:20:50). This solution was further diluted with MeOH:2PrOH:0.2%FA (30:20:50), infused through a fused silica capillary and sprayed through a PicoTip. The spray voltage was set to 3 kV, the cone voltage was set to 50 V and the source temperature to 80 °C. Nano-ESI-MS analysis was performed on a Synapt G2_Si mass spectrometer and the data was recorded with MassLynx 4.2. Mass spectra were acquired in the positive-ion mode by scanning the m/z range from 400 to 5000 Da with a scan duration of 1 s and an interscan delay of 0.1 s. The recorded m/z data was deconvoluted into mass spectra by applying the maximum entropy algorithm MaxEnt1.

SEC-MALS

SEC-MALS was performed to assess the oligomeric state of rXKR9. 10 µg of purified rXKR9 was filtered through a 0.1 µm filter, injected onto a Superdex 200 Increase 3.2/300 GL column, and run on an Agilent 1260 Infinity II HPLC, equilibrated in LMNG SEC buffer at room temperature. The HPLC was coupled to static light scattering detectors. Data was analyzed in the ASTRA software package. The dn/dc values used were 0.19 ml/g for rXKR9 and 0.132 ml/g for LMNG.

Liposome reconstitution and scrambling assay

Chloroform-solubilized soybean polar extracts (79.5%) and tail-labelled NBD-PE or NBD-PS (0.5%, wt/wt) were pooled together with cholesterol (20%, mol/mol). Chloroform was evaporated under a nitrogen stream. Lipids were washed once in chloroform and once in diethyl ether, before drying in a desiccator overnight. The next day, the lipid film was solubilized in liposome buffer (20 mM HEPES pH 7.5, 300 mM KCl, 2 mM EGTA), supplemented with 35 mM CHAPS, to a concentration of 20 mg/ml. Solubilized lipids were aliquoted, flash-frozen in liquid N₂, and stored at -80 °C. Other lipid compositions tested were 100% soybean polar lipids, 3 POPC:1 POPG (wt/wt), and 3 POPE:1 POPG (wt/wt). The lipids were prepared as described above.

On the day of purification, solubilized lipids were thawed at room temperature and diluted to 4 mg/ml in liposome buffer. Purified protein, either caspase-3 cleaved or un-cleaved, was added to lipids at a lipid to protein ratio of 100:1 (wt/wt) and incubated at room temperature for 15 minutes under gentle agitation. For empty liposome controls, an equal amount of SEC buffer was added to the lipids instead of protein. For detergent removal and formation of proteoliposomes, SM-II bio beads (20 mg per 1 mg lipids) were added to the lipid-protein mix. After 30 minutes incubation under constant agitation at room temperature, another batch of bio beads was added and the mix was transferred to 4 °C. After one hour, the third fraction of bio beads was added and the reconstitution mix was incubated at 4 °C overnight, constantly agitating. The next morning, a final batch of bio-beads was added and incubated for 4 h at 4 °C. Proteoliposomes were transferred to room temperature and filtered through gravity-flow columns to remove the bio beads. To harvest the proteoliposomes, they were centrifuged at 170'000 g for 30 minutes at 22 °C. Pelleted proteoliposomes were re-suspended in liposome buffer to 10 mg/ml and either flash-frozen in liquid N₂ and stored at -80 °C or incubated with caspase-3 and 1mM TCEP at room temperature overnight. After caspase-3 cleavage, the

proteoliposomes were also flash-frozen and stored at -80 °C. All steps were carried out in the dark to prevent bleaching of NBD fluorophores.

The scrambling measurement was essentially performed as described for TMEM16scramblases, without the addition of calcium (Alvadia et al., 2019; Brunner et al., 2014; Kalienkova et al., 2019). On the day of measurement, the proteoliposomes were thawed at room temperature, subjected to two more freeze-thaw cycles and extruded 21 times through a 200nm polycarbonate membrane, using Avanti MiniExtruder. Extruded proteoliposomes were diluted in 80 mM HEPES pH 7.5, 300 mM KCl, 2 mM EGTA to 0.2 mg/ml and initial fluorescence was recorded using a Spectrofluorometer (Ex.: 470nm, Em.: 530nm). After 60 s of measurement, 30 mM sodium dithionite was added and the measurement was continued for 360 s. The fluorescent decay was plotted as F/F_{\max} . Reconstitution efficiency was examined by re-extraction of the protein with 1% DDM for one hour on ice. Extracted protein was injected onto a Superdex 200 Increase 5/150 GL column, equilibrated in SEC buffer.

Purification, reconstitution, and characterization of mTMEM16F

mTMEM16F was essentially expressed, purified, and reconstituted into liposomes as described in (Alvadia et al., 2019). Briefly, mTMEM16F, with C-terminal 3C cleavage site, myc and SBP tags, was expressed in stably transfected mTMEM16F HEK293T cells by tetracycline induction (2 µg/ml) for 48h. Harvested cells were re-suspended in lysis buffer (20 mM HEPES pH7.5, 150 mM NaCl, 5 mM EGTA, 2% digitonin, protease inhibitor tablet), extracted for 2h, and centrifuged at 85'000 g for 30 min. The supernatant was incubated for 2h at 4 °C with streptavidin UltraLink resin (1 ml beads per 20 ml cell pellet). The resin was washed with 60 CV SEC buffer (20 mM HEPES pH7.5, 150 mM NaCl, 5 mM EGTA, 0.1% digitonin). Protein was eluted with 3 CV of SEC buffer, supplemented with 4 mM biotin, concentrated using 100 kDa cut-off concentrator, filtered through a 0.22 µm filter, and injected onto a Superose 6

10/300 GL column, pre-equilibrated in SEC buffer. Peak fractions were collected, concentrated and used for liposome reconstitution. mTMEM16F was reconstituted into liposomes composed of 79.5% soybean polar lipid extracts, 20% (mol/mol) cholesterol and 0.5% (wt/wt) 18:1 06:0 NBD-PE, at a 1:100 protein-to-lipid ratio (wt/wt). Harvested liposomes were re-suspended in liposome buffer, supplemented with the correct amount of $\text{Ca}(\text{NO}_3)_2$ to obtain the desired concentrations of free Ca^{2+} , calculated with the online WEBMAXC calculator (Bers et al., 2010). After thawing and extrusion through a 400nm membrane, the proteoliposomes were diluted in 80 mM HEPES pH 7.5, 300 mM KCl, 2mM EGTA, plus Ca^{2+} , aiming for symmetric buffer conditions. NBD fluorescence was recorded as described for rXKR9.

XKR8/9-basigin co-purification

To investigate the protein-protein interaction of rXKR9 and rat basigin, rXKR9 in pcDxNSM3 and rat basigin in pcDxC3GM were co-expressed and -purified. hXKR8 and human basigin in the same vectors were used as a positive control (Suzuki et al., 2016). For transfection of adherent HEK293T cells, XKR DNA and basigin DNA was mixed in a 1:2 ratio and then mixed with PEI MAX 40 kDa in a 1:2.5 ratio. The mix, diluted in non-supplemented DMEM, was incubated at room temperature for 15 minutes and then added to the HEK293T cells, grown in FBS and penicillin/streptomycin supplemented DMEM. Immediately after adding the transfection mix, 3.5 mM valproic acid was added. Cells were incubated at 37 °C and 5% CO_2 . 48h post-transfection, cells were harvested, washed in PBS, flash-frozen in liquid N_2 and pellets stored at -80 °C.

XKR-basigin complexes were essentially purified as described in the protein purification section. HRV 3C cleavage was not performed to maintain the fluorescent tag. In-gel fluorescence was monitored with a Viber Fusion FX7 imaging system (Ex.: 515nm, Em.: 530nm). Silver staining was performed according to manufacturer's instructions.

520

521 **Protein biotinylation**

522 For sybody selection and ELISA, purified rXKR9 was chemically biotinylated using EZ-link™
 523 NHS-PEG4-biotin. rXKR9 was concentrated to 2 mg/ml and incubated with a 10x molar excess
 524 of EZ-link™ NHS-PEG4-biotin for one hour on ice. The amine-reactive reaction was quenched
 525 by the addition of 5 mM Tris-HCl pH 7.5. Excess biotin was separated from biotinylated protein
 526 on a PD-10 desalting column. Eluted protein was concentrated to 1.3 mg/ml, mixed with
 527 glycerol to a final concentration of 10%, aliquoted, flash-frozen in liquid N₂, and stored at -80
 528 °C.

529

530 **Sybody selection and ELISA**

531 The sybody selection was performed as described previously (Zimmermann et al., 2020). The
 532 synthetic mRNA libraries, termed concave (CC), loop (LP), and convex (CX), and vectors
 533 needed for selections were generously provided by Prof. Markus Seeger, Institute of Medial
 534 Microbiology, University of Zurich. Selection and ELISA were performed in stated buffers
 535 with the addition of LMNG, where indicated. Briefly, one round of ribosome display was
 536 performed using the three different mRNA libraries, each encoding for 10¹² different binders.
 537 The output library of ribosome display was cloned into a phagemid vector, which was used for
 538 two successive rounds of phage display. During the second round of phage display, an off-rate
 539 selection was performed to remove binders with a high off-rate. Eluted phages were quantified
 540 by qPCR, which allowed to derive the enrichment. Enrichment was calculated based on the
 541 ratio of eluted phages from rXKR9 divided by the elution from the negative control,
 542 biotinylated TM287/288, purified as described previously (Hutter et al., 2019). Enrichment
 543 factors after the second round of phage display were 1.7, 8.3, and 1.1 for CC, LP, and CX
 544 libraries. Despite the low enrichment factors, the libraries were subcloned by FX-cloning into

pSb_init and expressed in 96-well plates. The periplasmic extract was subjected to ELISA in a 384-well format, using 50 µl biotinylated rXKR9 and TM287/288 as control at 50 nM per well. ELISA hits were sequenced by Sanger sequencing (Microsynth). Out of 64 hits, 21 clones were tested for expression and biochemical behavior.

Cryo-EM sample preparation and data collection

For the un-cleaved cryo-EM sample, rXKR9 was purified as described above, but purified sybody Sb1^{XKR9} was added to rXKR9 prior to injecting onto the Superdex 200 10/300 GL column in a 1.5x molar excess. The SEC-purified complex was concentrated using a 50 kDa cut-off concentrator to 1.5 mg/ml and applied to glow-discharged (0.39 mbar, 15 mA, 30 s) holey carbon grids (QuantiFoil R1.2/1.3 Au 200 mesh). Surplus sample was blotted off for 2-4 seconds with zero blotting force in a controlled environment (4 °C, 100% relative humidity) using Vitrobot Mark IV. The sample was plunge-frozen in a liquid ethane-propane mix and stored in liquid N₂ until data collection.

For the cleaved cryo-EM sample, rXKR9 was purified as described above. After SEC, the protein was concentrated to 0.87 mg/ml and incubated with 24 units of caspase-3 and 10 mM DTT overnight on ice. The next day, purified sybody Sb1^{XKR9} was added in a 1.5x molar excess and complexes were subjected to SEC on a Superdex 200 10/300 GL column pre-equilibrated in SEC buffer. The cleaved complex was concentrated to 1.5 mg/ml and plunge-frozen the same way as the un-cleaved sample.

The hXKR8-hBSG complex was purified as described below. The complex was concentrated to 2 mg/ml and plunge-frozen the same way as the rXKR9 samples.

All rXKR9 samples were imaged on a Titan Krios G3i, operated at 300 kV, with a 100 µm objective aperture. All data were recorded using a post-column BioQuantum energy filter with a 20 eV slit and a K3 Summit direct electron detector in super-resolution mode. Dose-

fractionated micrographs were recorded with a defocus range of -1 μm to -2.4 μm in an automated mode using EPU 2.9. The datasets were acquired at a nominal magnification of 130'000x, corresponding to a pixel size of 0.651 \AA per pixel (0.3255 \AA per pixel in super-resolution mode), with 1.01 s exposure (36 frames) and a dose of 1.94 $\text{e}^-/\text{\AA}^2/\text{frame}$ and 1.93 $\text{e}^-/\text{\AA}^2/\text{frame}$ for the un-cleaved dataset and cleaved dataset, respectively. This resulted in a total electron dose of approximately 70 $\text{e}^-/\text{\AA}^2$ on the level of the specimen.

The hXKR8-BSG sample was imaged on a 300 kV Tecnai G² Polara microscope, with a 100 μm objective aperture. All data were collected using a post-column quantum energy filter with a 20 eV slit and a K2 Summit direct electron detector in counting mode. SerialEM 3.7 was used to set up automated data collection of dose-fractionated micrographs, with a defocus range of -0.8 μm to -2.5 μm . The dataset was recorded at a nominal magnification of 130'000x, corresponding to a pixel size of 1.34 \AA per pixel, with a total exposure of 12.4 s (31 frames) and a dose of 1.1 $\text{e}^-/\text{\AA}^2/\text{frame}$, which resulted in a total electron dose of approximately 35 $\text{e}^-/\text{\AA}^2$ on the level of the specimen.

Cryo-EM data processing

Data processing of XKR9 was performed entirely in cryoSPARC v.3.0.1 and v.3.2.0 (Punjani et al., 2017). For the un-cleaved dataset, 12'396 micrographs were collected and subjected to patch motion correction and patch CTF estimation. Micrographs were Fourier-cropped once during motion correction, resulting in a pixel size of 0.651 \AA per pixel. Bad micrographs were discarded, based on CTF fit resolution, relative ice thickness, and total full-frame motion, resulting in 9'823 good micrographs. A small subset of micrographs was used for blob picking, using a blob with 50 \AA to 120 \AA diameter. Particles were extracted with a box size of 360 pixel and Fourier-cropped to 180 pixels (1.302 \AA per pixel). From two rounds of 2D classification, with marginalization over poses and shifts and a circular 150 \AA mask, 2D class averages

showing protein features were used as templates for automated template-based picking from all good micrographs. Particles were extracted as described above. After two rounds of 2D classification, 2'171'713 particles were subjected to *ab initio* reconstruction with five classes, no similarity, C1 symmetry, and initial alignment resolution of 12 Å. 1'852'344 particles, from classes with protein features were directed into a second *ab initio* reconstruction with three classes, no similarity, C1 symmetry, and 7 Å initial resolution. The best-resolved class, together with the worst-resolved class from the first *ab initio*, were used as references for three rounds of heterogeneous refinement together with the particle set selected from the first round of *ab initio* reconstruction. After heterogeneous refinement, where the initial resolution of the input volumes was set to 7 Å, 866'439 good particles were locally CTF refined. Subsequently, the particles were further refined in a non-uniform (NU) refinement (Punjani et al., 2020), using C1 symmetry, yielding a map with a 3.66 Å resolution, according to the 0.143 cut-off criterion (Rosenthal and Henderson, 2003). During NU-refinement, the resolution of the input structure was filtered to 12 Å and per-group CTF parameters were optimized. The directional resolution estimation was done using the 3DFSC server (Tan et al., 2017) and local resolution estimation within the cryoSPARC environment.

For cleaved rXkr9, 14'929 micrographs were collected and similarly motion-corrected, CTF-estimated and curated as the micrographs from the un-cleaved dataset. This resulted in 12'135 good micrographs, that were used for template-based picking, using templates created from the 3.66 Å map from the un-cleaved dataset. Particles were extracted as described previously. After two rounds of 2D classification, 834'105 and 496'296 particles were used for a first and second *ab initio* reconstruction with the same parameters as for the un-cleaved dataset. All particles used for the second round of *ab initio* were subjected to five rounds of heterogeneous refinement, using the same parameters as described above. The best-resolved class from the second *ab initio* reconstruction and a decoy class, generated from de-selected particles from 2D classifications, were used as input volumes. Analogously, particles were refined in a local CTF

refinement and a NU-refinement, yielding a map at 4.3 Å.

The hXkr8-hBSG data was processed in RELION 3.0.7 (Zivanov et al., 2018). 2'212 micrographs were collected and motion-correction using MotionCor2 v.1.2.3 (Zheng et al., 2017). After CTF estimation, performed using CTFFIND4.1 (Rohou and Grigorieff, 2015), micrographs with a resolution higher than 6 Å were discarded, resulting in 2'054 good micrographs. 1'000 particles were manually picked, extracted with a box size of 160 pixel, binned to 80 pixels (2.68 Å per pixel), and subjected to an initial 2D classification. 2D classes showing protein features were used for auto-picking. 465'373 particles were extracted as described above and directed into four rounds of 2D classification. 282'197 particles were used to generate an initial 3D model and then subjected to one round of 3D classification. The most promising class was refined in a 3D refinement, yielding a low-resolution structure at 15.3 Å.

Model building and refinement

The models of full length rXKR9 and caspase-cleaved rXKR9 were built in Coot (Emsley and Cowtan, 2004). Full length rXKR9 was built *de novo* into the cryo-EM density and cleaved rXKR9 was built using the full-length structure as reference. The cryo-EM density of full length rXKR9 was of sufficiently high resolution to unambiguously assign residues 1-66, 81-105, 119-344 and 365-373. Sb1^{XKR9} was initially modeled based on the high resolution structure of a nanobody (PDB: 1ZVH), with CDR3, which interacts with the membrane protein, being rebuilt into the cryo-EM density. The atomic models were improved iteratively by cycles of real-space refinement in PHENIX (Afonine et al., 2018) with secondary structure constraints applied followed by manual corrections in Coot. Validation of the models was performed in PHENIX. Surfaces were calculated with MSMS (Sanner et al., 1996). Figures and videos containing molecular structures and densities were prepared with DINO (<http://www.dino3d.org>), Chimera (Pettersen et al., 2004), and ChimeraX (Pettersen et al., 2021).

Acknowledgements

This work was supported by a grant of the European Research Council (ERC no 339116, AnoBest) to Raimund Dutzler and a Candoc grant of the Forschungskredit of the University of Zurich (grant no FK-20-040) to Monique. S. Straub. The contribution of Janine D. Brunner and Stephan Schenck to the preparation and evaluation of XKR constructs prior to the described study is acknowledged. The cryo-electron microscope and K3-camera were acquired with support of the Baugarten and Schwyzer-Winiker foundations and a Requip grant of the Swiss National Science Foundation (No. 316030_183382). We thank Simona Sorrentino and the Center for Microscopy and Image Analysis (ZMB) of the University of Zurich for the support and access to the electron microscope, S. Rutz for help during data collection and Markus A. Seeger for providing the sybody libraries. All members of the Dutzler lab are acknowledged for their help at various stages of the project.

Competing interests

The authors declare no competing interests.

Accession codes

The cryo-EM density maps of full-length and caspase-cleaved XKR9 have been deposited in the Electron Microscopy Data Bank under ID codes EMD-xxxx and EMD-xxxx, respectively. The coordinates for the atomic model of full-length XKR9 refined against the 3.66 Å cryo-EM density and the coordinates of caspase-cleaved XKR9 refined against the 4.3 Å cryo-EM density have been deposited in the Protein Data Bank under ID codes YYYY and ZZZZ.

Author Contributions

M.S.S. purified proteins, selected sybodies, prepared samples for cryo-EM, collected cryo-EM Data and proceeded with structure determination and functional experiments. C.A. has prepared expression constructs, carried out initial expression and purification screening and performed TMEM16F scrambling experiments. M.S. has assisted in collection and analysis of cryo-EM data. R.D. has assisted during structure determination. M.S.S. and R.D. jointly planned experiments, analyzed the data and wrote the manuscript.

Author Information

The authors declare no competing financial interests. Correspondence and requests for materials should be addressed to R.D. (dutzler@bioc.uzh.ch).

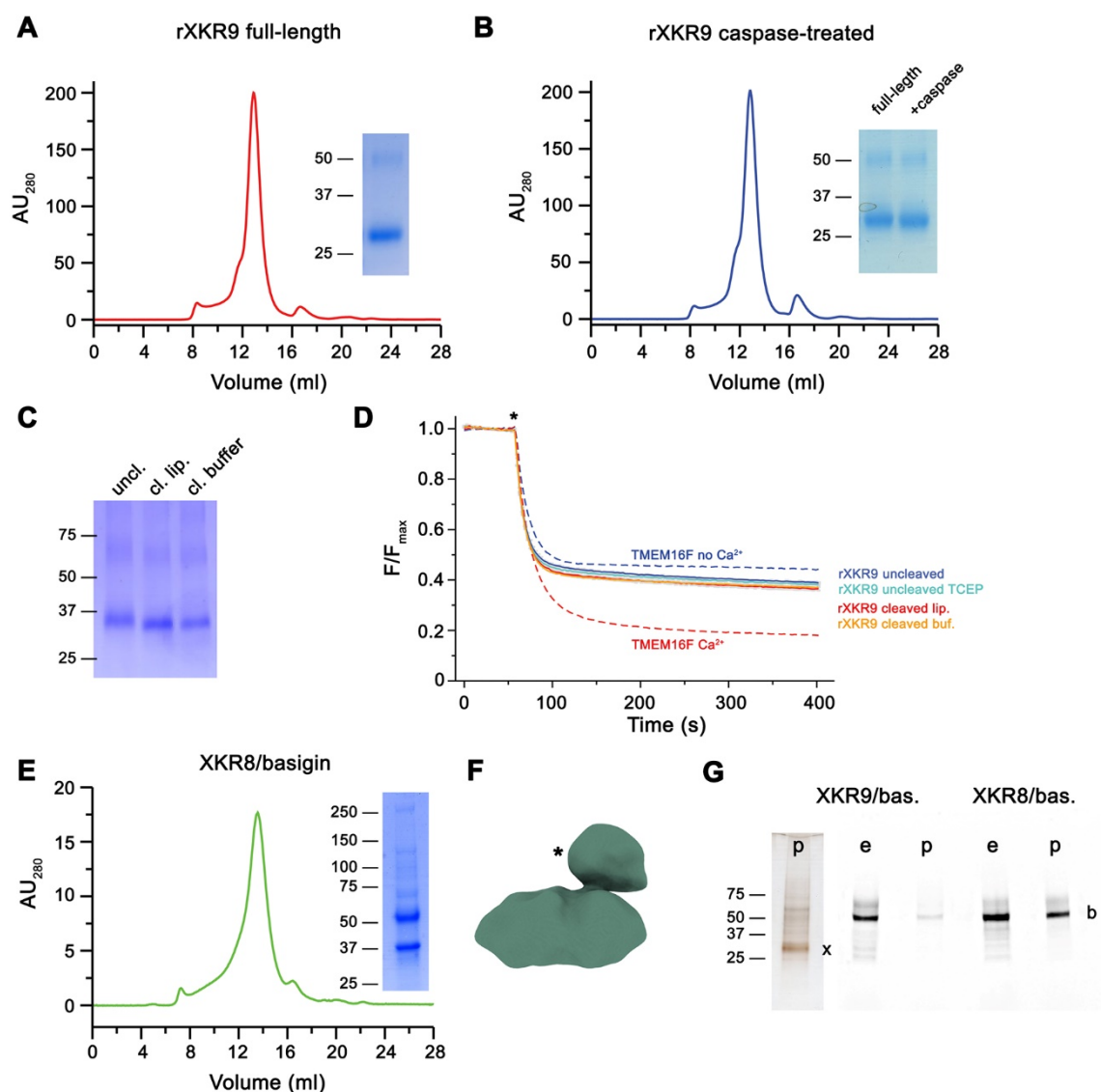


Figure 1. Biochemical and functional properties of rXKR9. Size exclusion chromatogram of full-length (A) and caspase-treated (B) rXKR9. Insets show SDS-PAGE gel of the pooled and concentrated peak sample. (C) SDS-PAGE gel of rXKR9 extracted from different proteoliposome preparations used for lipid scrambling assays. The samples treated with caspase-3 in liposomes (cl. lip.) or detergent solution prior to reconstitution (cl. buffer) show shift towards smaller molecular weight compared to the full-length protein (uncl.). (D) Assay to monitor the protein-catalyzed movement of fluorescent lipids between both leaflets of a bilayer. The addition of the reducing agent dithionite to the solution (*) is indicated. Traces of TMEM16F in absence and presence of 100 μ M Ca^{2+} displayed in Fig. 1. — figure supplement

1D are shown as controls for an inactive and active scramblase, respectively (dashed lines). No pronounced activity is observed in any of the liposome preparations containing either full-length or caspase-3-treated samples. Data show mean and standard deviations of three technical replicates. (E) Purification of a human XKR8-basigin complex. Left, size exclusion chromatogram of hXKR8 in complex with basigin containing a GFP fusion. The complex was purified via a tag attached to hXKR8. SDS-PAGE gel showing the Coomassie stained bands of the purified complex (right). (F) Low resolution reconstruction of the hXKR8-basigin complex. The density protruding from the membrane-inserted part (*) corresponds to the extracellular part of basigin. (G) In gel-fluorescence showing GFP-tagged basigin (b) in whole-cell extracts (e) and after affinity purification (p) of hXKR8 and rXKR9. Whereas the XKR8 samples show a pronounced basigin band, the XKR9 samples only contain traces of the protein. The presence of XKR9 in the sample (marked with 'x') is shown on silver-stained SDS-PAGE gel (left). The concentration of XKR8 after pulldown is several-times lower as judged by its barely detectable band on the same gel (not shown). (A-C, E, G) Molecular weight (kDa) of marker proteins on SDS-PAGE gels are indicated.

The following figure supplements are available for figure 1:

Figure supplement 1. Biochemical characterization of rXKR9.

Figure supplement 2. Low-resolution cryo-EM reconstruction of a hXKR8-basigin complex.

Figure supplement 3. Preparation of rXKR9-Sb1^{XKR9} complexes.

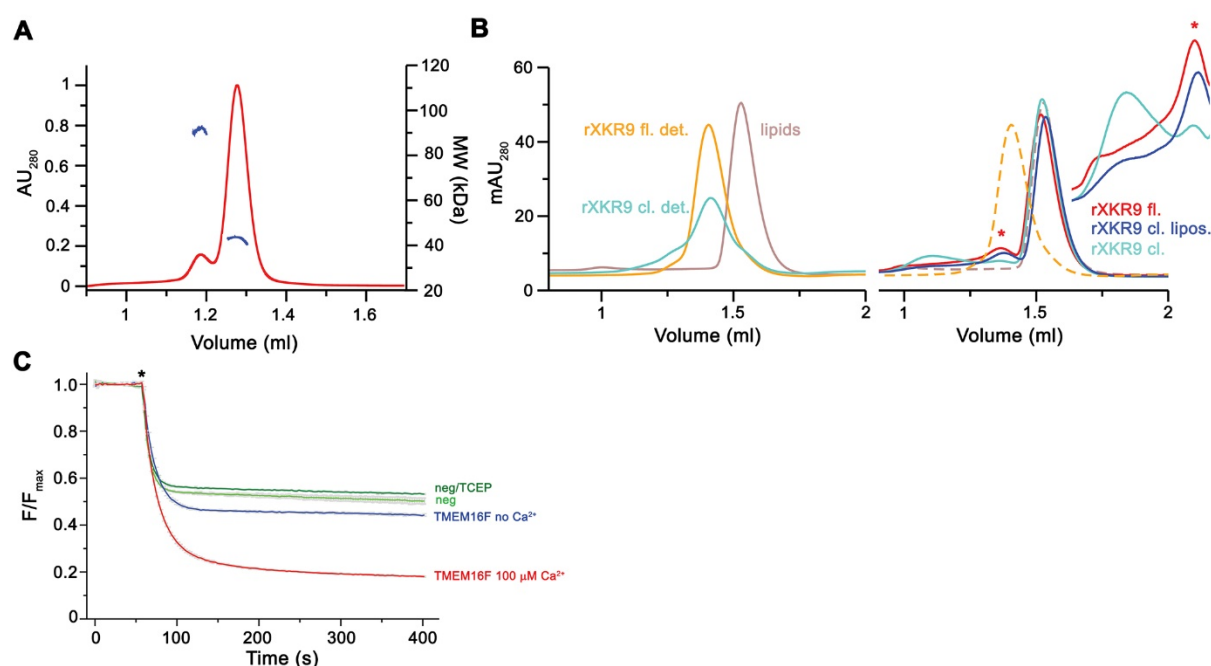


Figure 1—figure supplement 1. Biochemical characterization of rXKR9. (A) Multi-angle light scattering coupled to size-exclusion chromatography of detergent-solubilized rXKR9. Continuous red trace corresponds to the absorption at 280 nm. The corrected molecular weights of the protein components of monomeric rXKR9 (43.4 kDa) and traces of a dimer are shown in blue. (B) Size exclusion chromatogram of detergent-solubilized proteoliposomes containing reconstituted rXKR9 constructs used for scrambling experiments shown in Figure 1C, D. Left, chromatograms of detergent-solubilized full-length (rXKR9 fl. det.) and caspase treated (rXKR9 cl. det.) proteins used for reconstitution and solubilized liposomes (lipids) for the determination of the elution volumes of protein and lipid components. Right, size exclusion chromatograms of solubilized proteoliposomes of full-length (rXKR9 fl.) and samples treated with caspase-3 before (rXKR9 cl.) and after reconstitution (rXKR9 cl. lipos.). Peak of monomeric protein (*) is indicated. Elution profiles of reference protein and lipid samples are shown as dashed lines for comparison. Inset shows scaled regions of protein peaks and aggregates, which are pronounced in the sample of rXKR9 treated with caspase-3 prior to reconstitution. (C) Assay to monitor the protein-catalyzed movement of fluorescent lipids between both leaflets of a bilayer. The addition of the reducing agent dithionite to the solution

(*) bleaches the fluorescent groups located in the outer leaflet, which leads to a decrease of the initial fluorescence to about half (45-55% depending on the preparation) in absence of scrambling activity and a further reduction in case of lipid flip-flop. Traces of TMEM16F in absence and presence of 100 μM Ca^{2+} are shown as example for an inactive and an active scramblase. Traces of liposomes without protein, in presence and absence of 1 mM TCEP are displayed for comparison. Data show mean and standard deviations of three technical replicates.

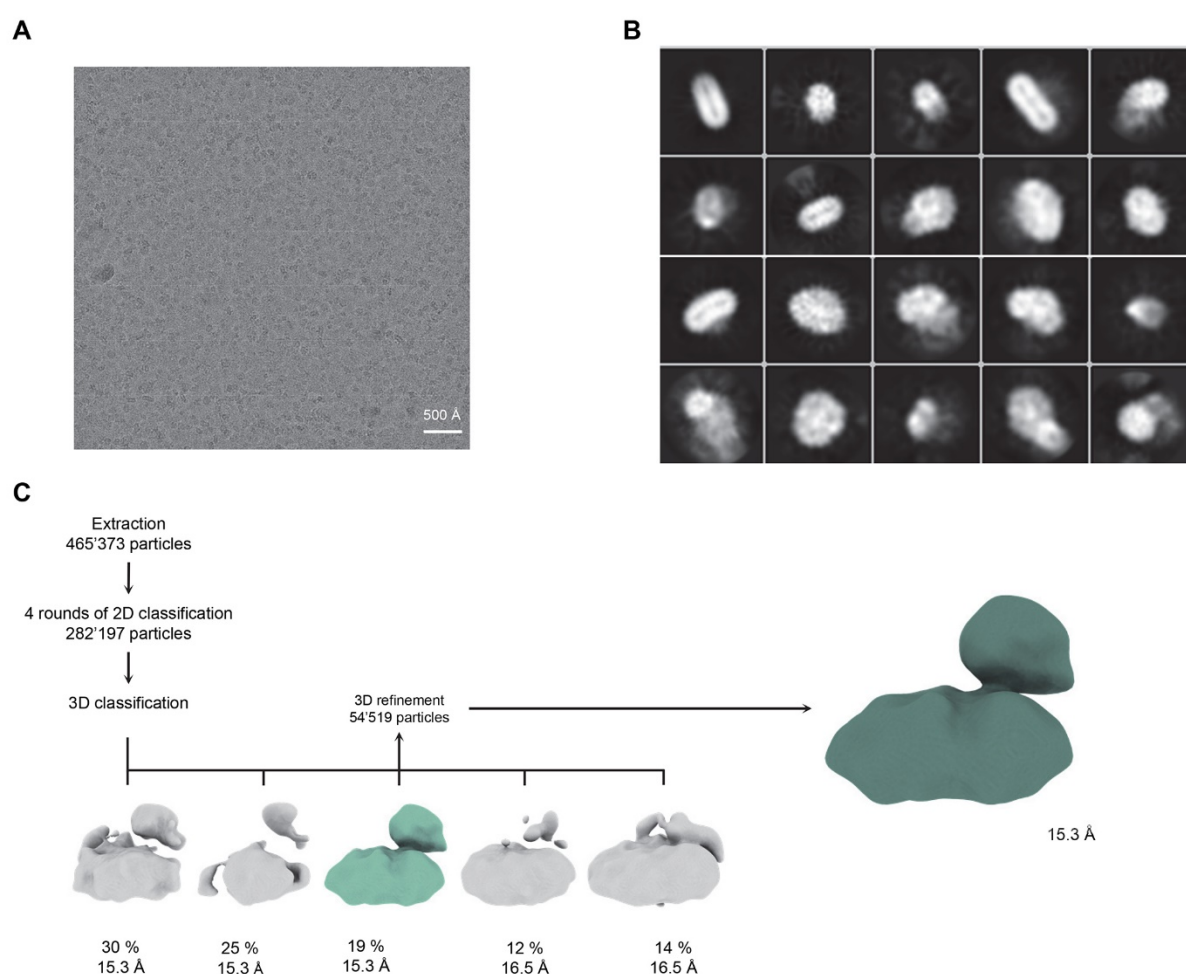


Figure 1—figure supplement 2. Low-resolution cryo-EM reconstruction of a hXKR8-basigin complex. (A) Representative cryo-EM micrograph acquired with a Tecnai G² Polara microscope and a K2 summit camera. (B) 2D class averages of a hXKR8-basigin complex. (C) Data processing workflow. After extraction and four rounds of 2D classification, a 3D

classification with five classes was performed. The class with protein-like features (highlighted in color) was used as an input for 3D refinement with C1 symmetry, which yielded a 15.3 Å map. The percent of particles and resolution of each class is indicated.

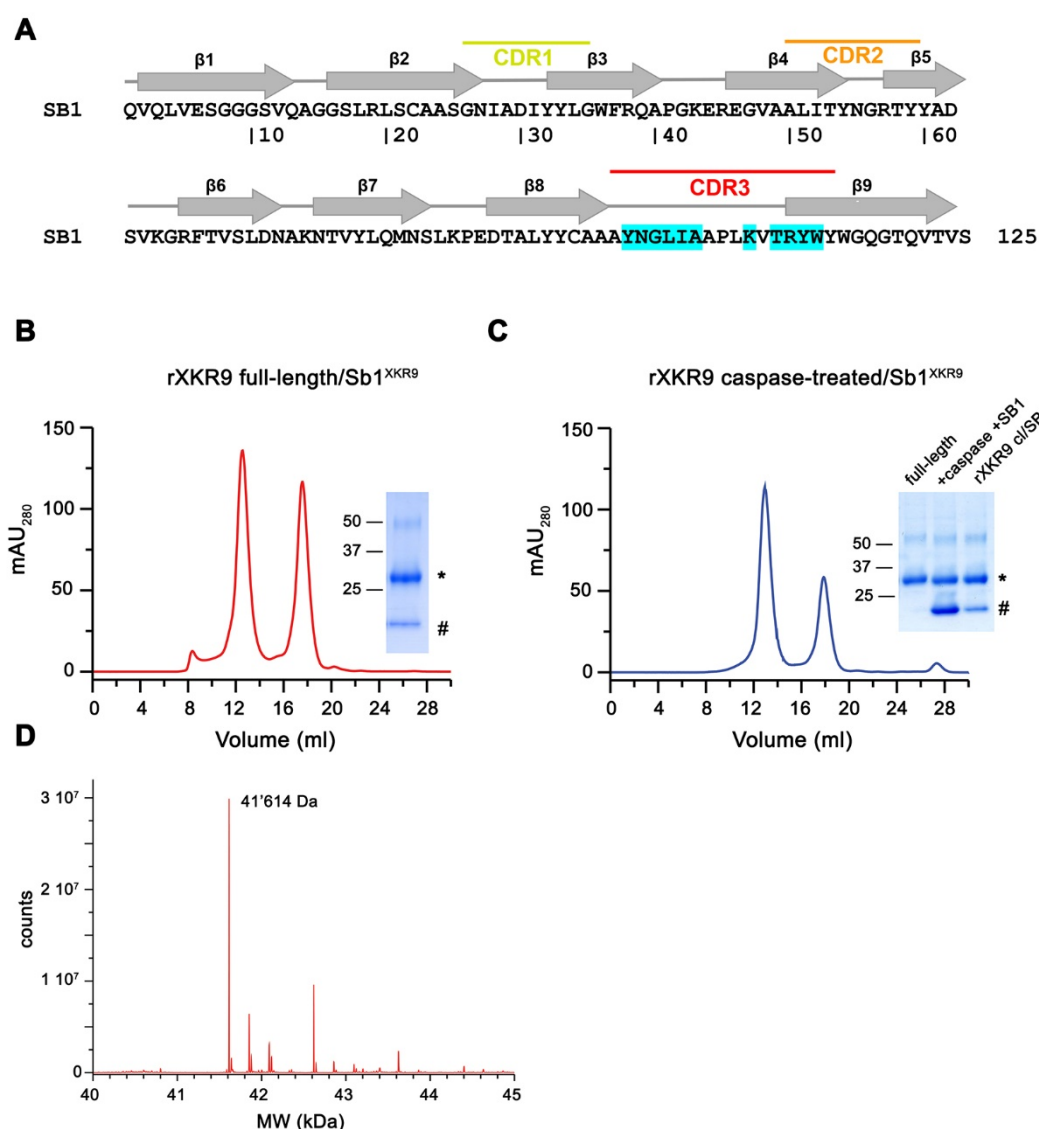


Figure 1—figure supplement 3. Preparation of rXKR9-Sb1^{XKR9} complexes. (A) Sequence of the sybody Sb1^{XKR9}. Secondary structure and randomized complementary determining regions are indicated. Residues in contact with rXKR9 are highlighted in cyan. Size exclusion chromatogram of full-length (B) and caspase-treated (C) rXKR9-Sb1^{XKR9} used for cryo-EM analysis. Unbound sybodies added in excess are eluted as peak with a retention volume of 18 ml. Insets show SDS-PAGE of the pooled and concentrated peak samples. rXKR9 and Sb1^{XKR9}

are marked by '*' and '#', respectively. '+caspase +SB1' refers to caspase treated sample incubated with excess sybody. 'rXKR9 cl/SB1' to the complex after SEC. (D) Section of the mass spectrum of the rXKR9-Sb1^{XKR9} complex confirming the reduced mass of rXKR9 after caspase treatment. The observed molecular weight (41'614 Da) matches the expected weight of the cleaved construct.

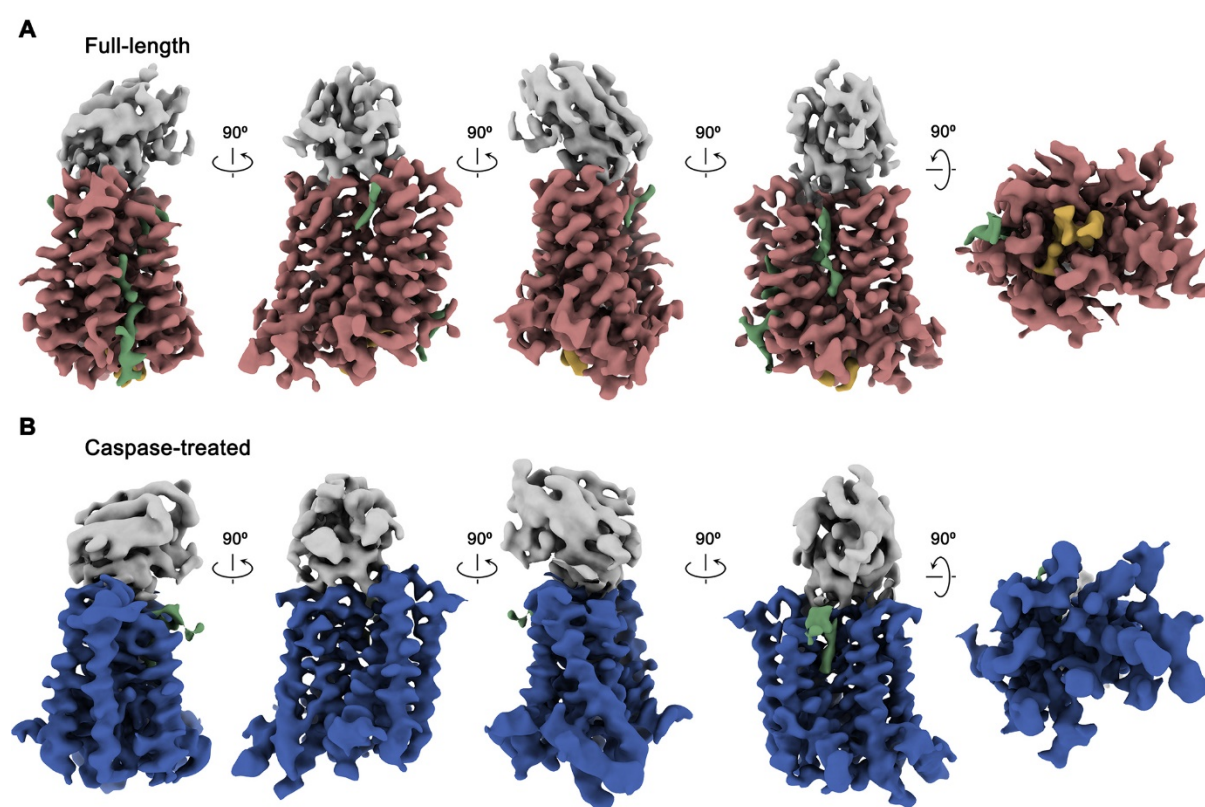
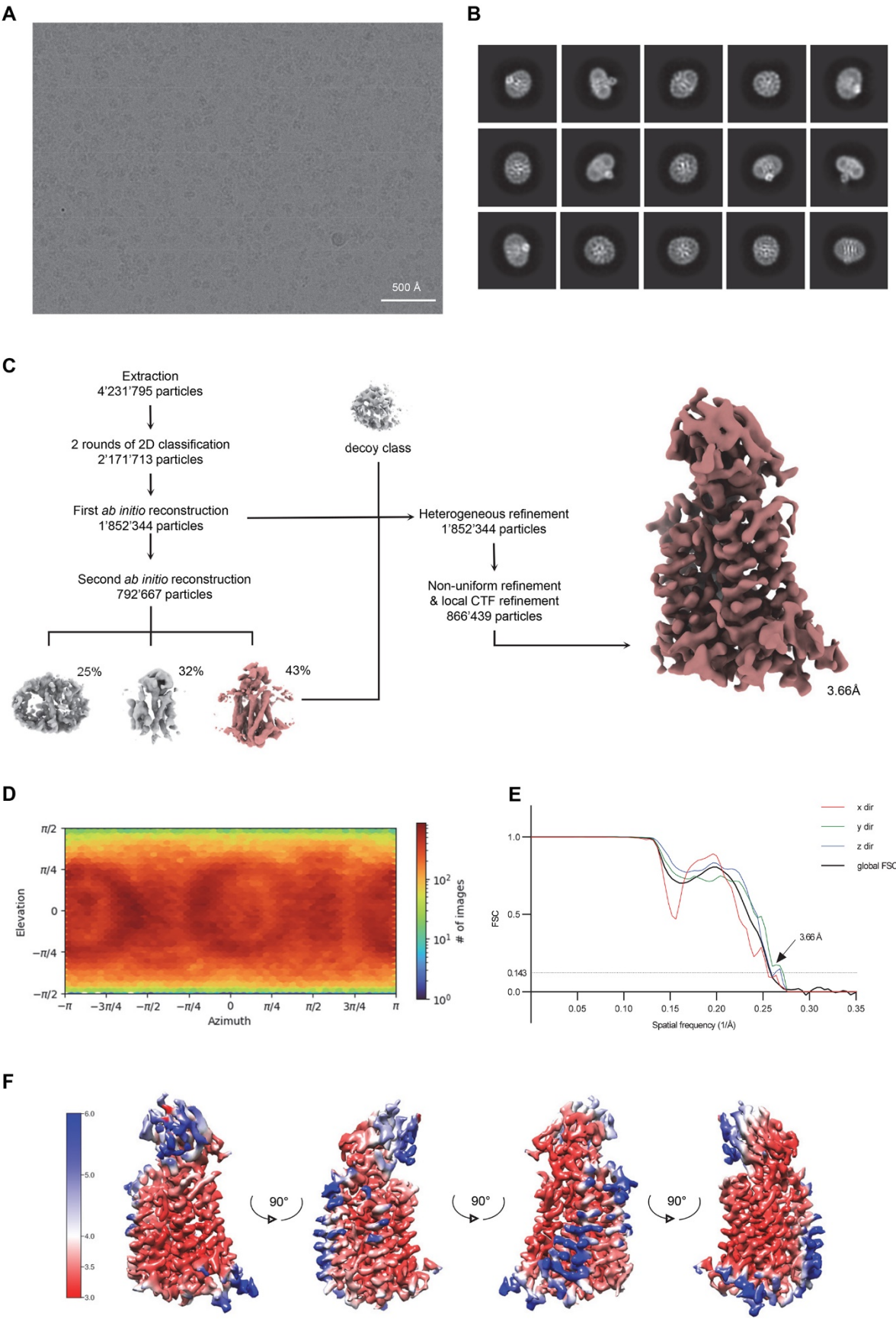


Figure 2. Cryo-EM maps of rXKR9-Sb1^{XKR9} complexes. (A) Cryo-EM density of complexes of the full-length construct at 3.66 Å (contoured at 9.5 σ) and (B), the caspase-treated protein at 4.3 Å (contoured at 8.8 σ). The relationship between orientations is indicated. rXKR9 density is shown in unique colors, density of Sb1^{XKR9} is shown in grey, residual density that can be attributed to bound lipids in green. Density of the C-terminus of full-length protein (A) is colored in orange.

764 **Figure supplement 1.** Cryo-EM reconstruction of the full-length rXKR9-Sb1^{XKR9} complex.

765 **Figure supplement 2.** Cryo-EM reconstruction of the caspase-treated rXKR9-Sb1^{XKR9}
766 complex.

767 **Figure supplement 3.** Cryo-EM density.



768

769 **Figure 2—figure supplement 1.** Cryo-EM reconstruction of the full-length rXKR9-Sb1^{XKR9}
770 complex. (A) Representative micrograph of the complex acquired with a Titan Krios G3i
771 microscope equipped with a K3 camera. (B) 2D class averages of the rXKR9-Sb1^{XKR9} dataset.
772 (C) Data processing workflow. After extraction and two rounds of 2D classification, a first *ab*
773 *initio* reconstruction with five classes was performed (classes not shown). The particles classes
774 with protein-like features were used as an input for the second round of *ab initio* reconstruction.
775 The second *ab initio* reconstruction resulted in one class with distinct protein features
776 (highlighted in color). The particle distribution is indicated in %. The class with the highest
777 number of particles, together with a decoy class, and all the particles used for the second round
778 of *ab initio* reconstruction were subjected to three rounds of heterogeneous refinement. Non-
779 uniform refinement and local CTF-refinement with C1 symmetry yielded a map at a resolution
780 of 3.66 Å. (D) Angular distribution of particle orientations. The heatmap displays the number
781 of particles for a given viewing angle. (E) Directional and global FSC plots. The global FSC is
782 shown in black. Dashed line indicates 0.143 cut-off and the resolution at which the FSC curve
783 drops below 0.143 is indicated. The directional FSC curves providing an estimation of
784 anisotropy of the dataset are shown for directions x , y, and z. (F) Final 3D reconstruction of
785 the rXkr9-Sb1^{XKR9} complex in indicated orientations, colored according to the local resolution,
786 estimated in cryoSPARC v.3.2.0.

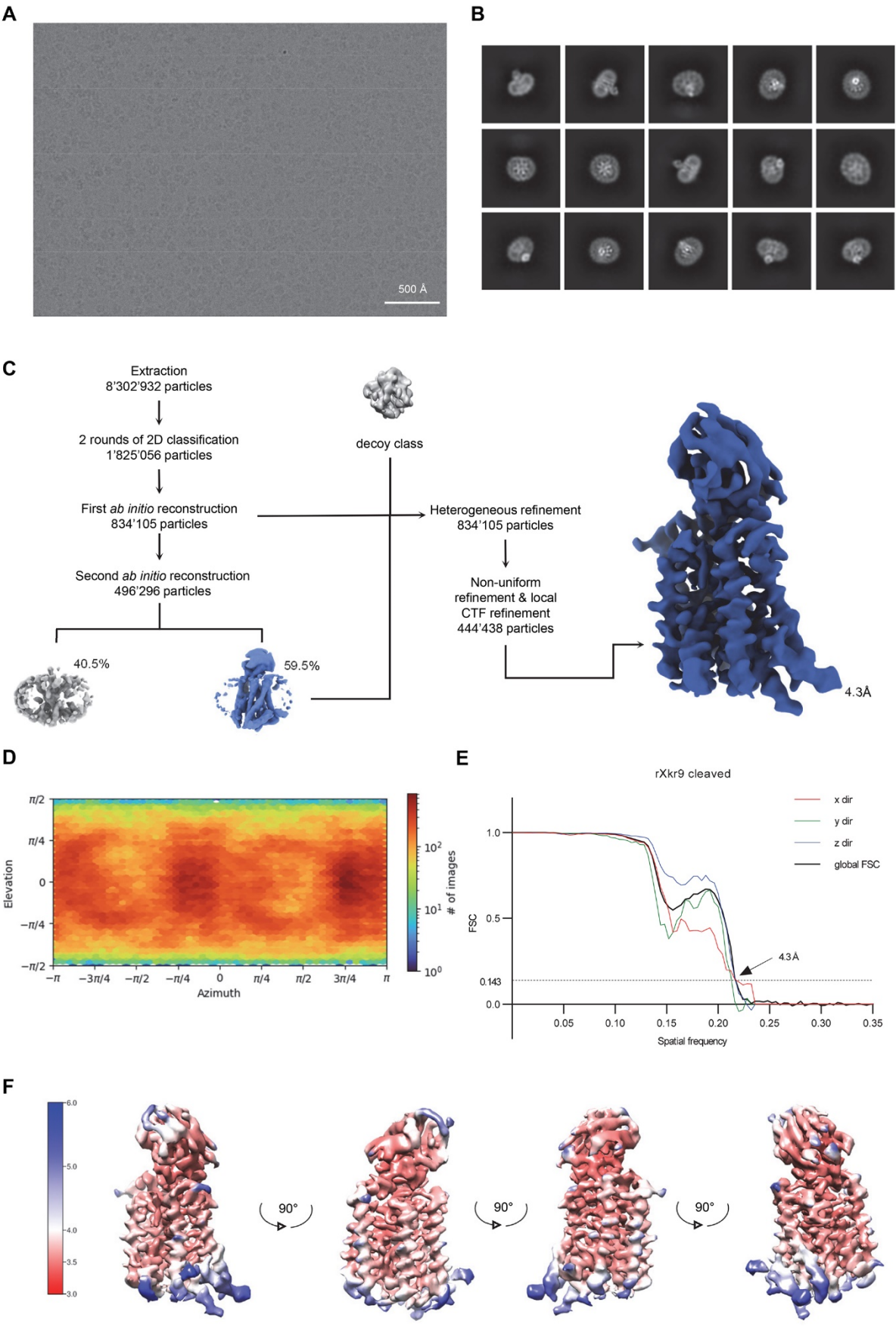


Figure 2—figure supplement 2. Cryo-EM reconstruction of the caspase-treated rXKR9-Sb1^{XKR9} complex. (A) Representative micrograph of the complex acquired with a Titan Krios G3i microscope equipped with a K3 camera. (B) 2D class averages of the caspase-treated rXKR9-Sb1^{XKR9} dataset. (C) Data processing workflow. After extraction and two rounds of 2D classification, a first *ab initio* reconstruction with five classes was performed (classes not shown). The particles classes, with protein-like features, were used as an input for the second round of *ab initio* reconstruction. The second *ab initio* reconstruction resulted in one class with distinct protein features (highlighted in color). The particle distribution is indicated in %. The class with the highest number of particles, together with a decoy class, and all the particles used for the second round of *ab initio* reconstruction were subjected to three rounds of heterogeneous refinement. Non-uniform refinement and local CTF-refinement with C1 symmetry yielded a map with a resolution of 4.3 Å. (D) Angular distribution of particle orientations. The heatmap displays the number of particles for a given viewing angle. (E) Directional and global FSC plots. The global FSC is shown in black. Dashed line indicates 0.143 cut-off and the resolution at which the FSC curve drops below 0.143 is indicated. The directional FSC curves providing an estimation of anisotropy of the dataset are shown for x, y, and z directions. (F) Final 3D reconstruction of the caspase-cleaved rXkr9-Sb1^{XKR9} complex in indicated orientations, colored according to the local resolution, estimated in cryoSPARC v.3.2.0.

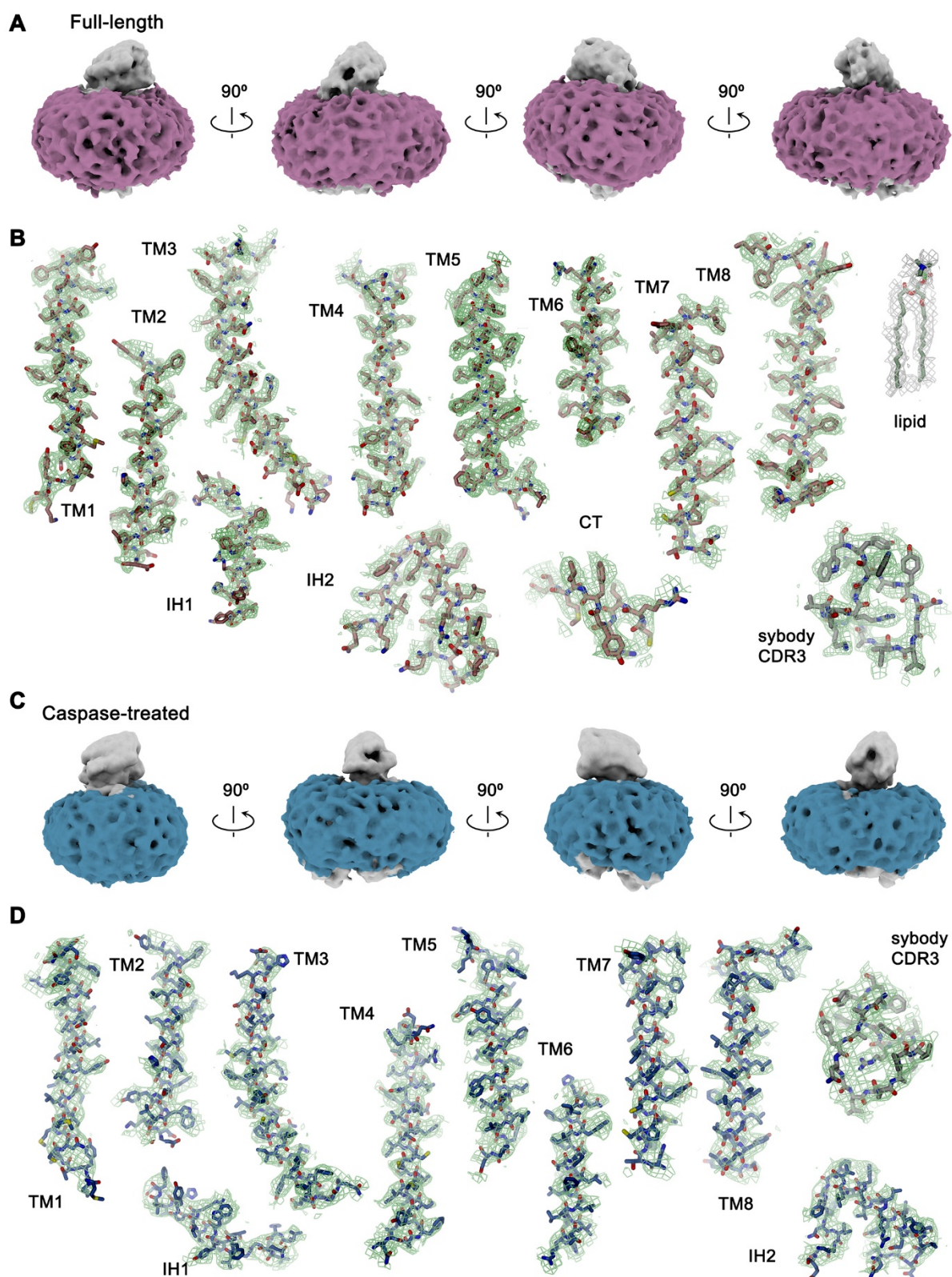


Figure 2—figure supplement 3. Cryo-EM density. (A) Density of the detergent belt (magenta) in the *ab initio* cryo-EM reconstruction of the full-length rXKR9-Sb1^{XKR9} complex (contoured at 5.8 σ). Relationships between orientations are indicated. (B) Sections of the cryo-EM density

(green, 8σ) superimposed on the refined structure of the full-length rXKR9-Sb1^{XKR9} complex 3.66 Å. Lipid refers to a phosphatidylcholine fitted into residual density (gray, 4σ). (C) Density of the detergent belt (blue) in the *ab initio* Cryo-EM reconstruction of the caspase-cleaved rXKR9-Sb1^{XKR9} complex (contoured at 6.7σ). Relationships between orientations are indicated. (D) Sections of the cryo-EM density (green, 7σ) superimposed on the refined structure of the caspase-cleaved rXKR9-Sb1^{XKR9} complex 4.3 Å.

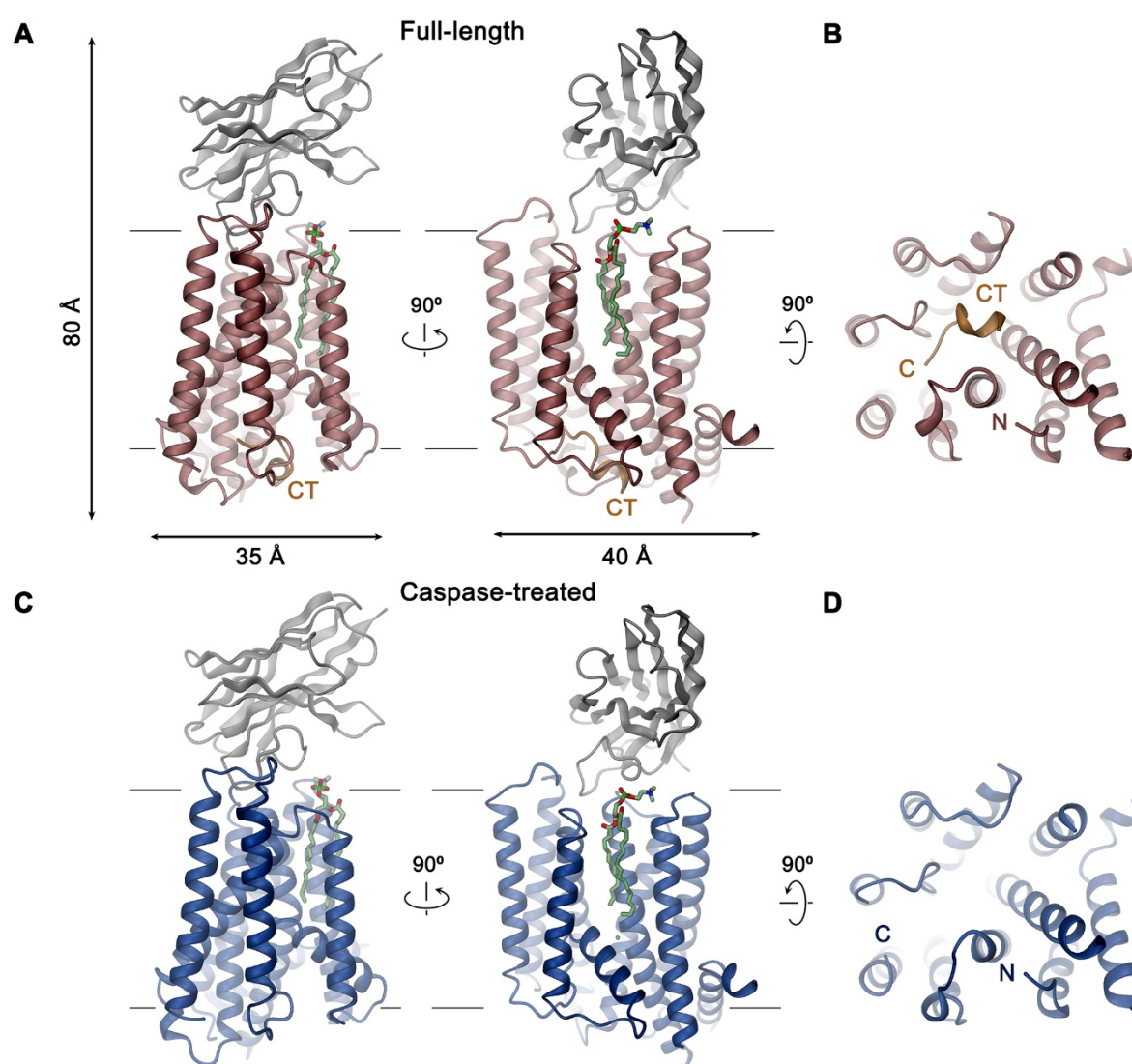


Figure 3. XKR9-SB1^{XKR9} complex. Ribbon representation of Sb1^{XKR9} complexes of (A, B) full-length and (C, D) caspase-treated rXKR9. The relationship between orientations is indicated. rXKR9 is shown in unique colors, Sb1^{XKR9} in grey, and the C-terminus of the full-

length protein (CT) that is cleaved upon caspase-3-treatment in orange. A bound lipid is shown in green as stick model. **A, C**, View is from within the membrane, with membrane boundaries indicated. **B, D**, View is from the cytoplasm.

Figure supplement 1. rXKR9-Sb1^{XKR9} interactions.

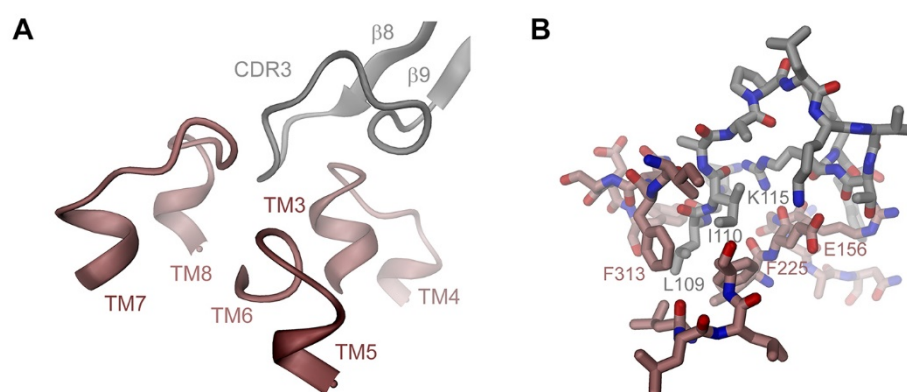


Figure 3—figure supplement 1. rXKR9-Sb1^{XKR9} interactions. (A) Ribbon representation of the rXKR9-Sb1^{XKR9} interaction interface. Color code is as in Figure 3A. Secondary structure elements and complementary determining regions are indicated. (B) Stick model of interacting residues. View as in A, with selected residues labeled.

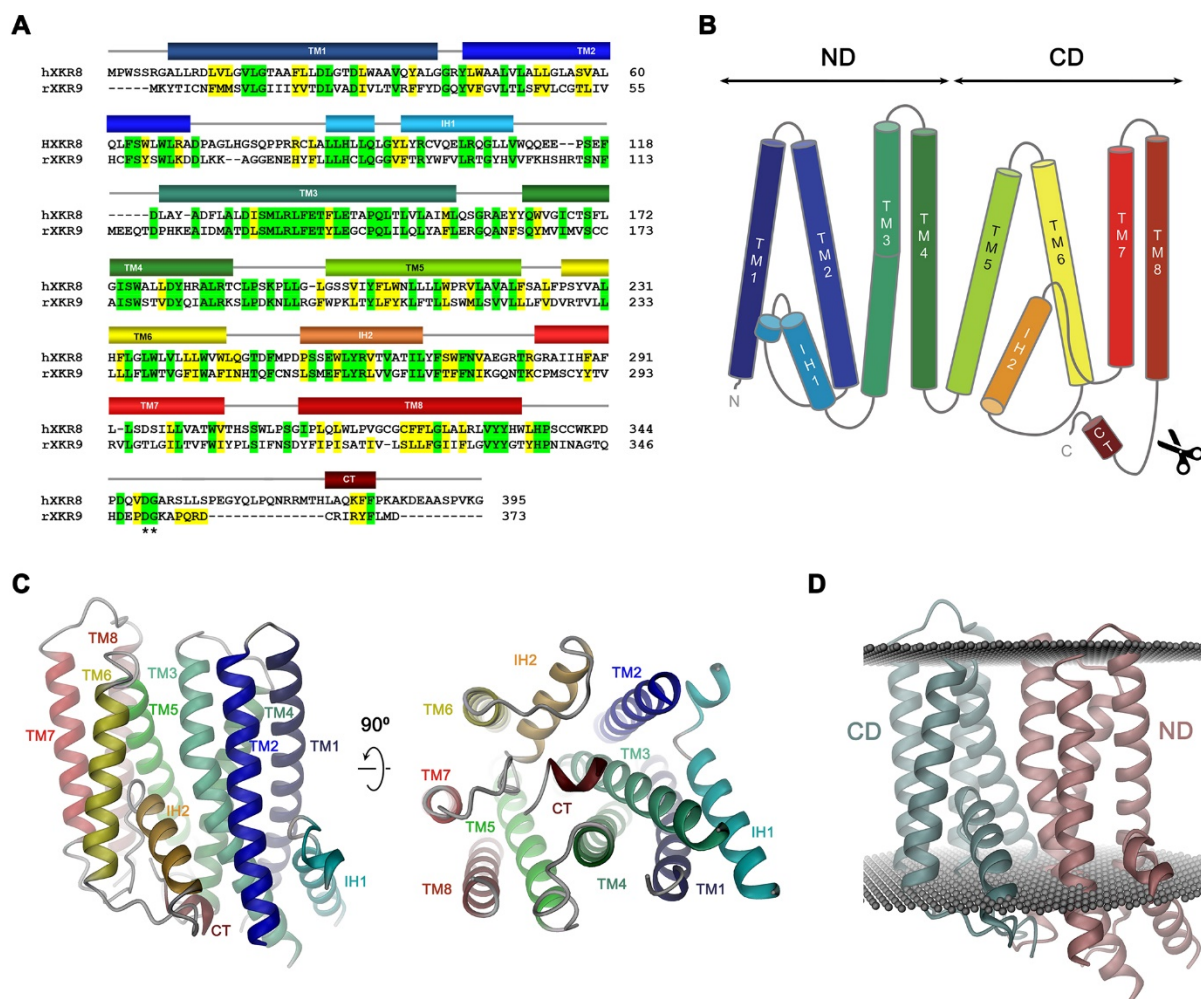
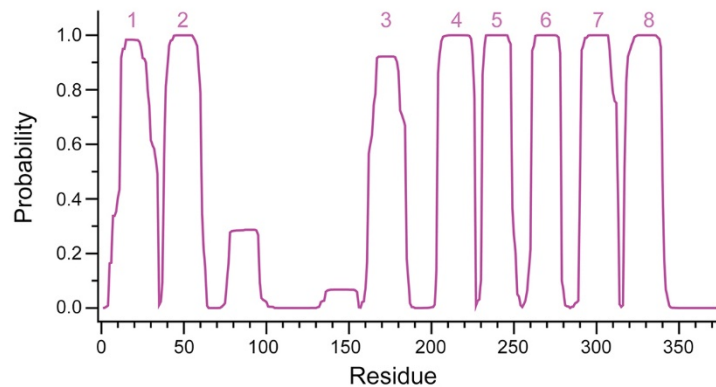


Figure 4. Sequence and Topology. Sequence alignment of human XKR8 (hXKR8, NCBI: NP_060523.2) and rXKR9 (NCBI: NP_001012229.1), secondary structure elements are indicated. Identical residues are highlighted in green, similar residues in yellow. The caspase-3 cleavage site is marked by *. **(B)** Schematic topology of rXKR9. ND and CD refer to N-terminal and C-terminal domain, respectively. Scissors indicate location of caspase cleavage site. **(C)** Ribbon representation of the rXKR9 subunit. The relationship between orientations is indicated. Color code is as in A and B. **(D)** Ribbon representation of rXKR9 with ND and CD shown in unique colors. Grey spheres indicate inner and outer boundaries of the hydrophobic core of the lipid bilayer.

Figure supplement 1. Hydropathy analysis of the rXKR9 sequence.

A



B



Figure 4—figure supplement 1. Hydropathy analysis of the rXKR9 sequence. **(A)** Prediction of membrane spanning helices (numbered) by the TMHMM server (Krogh et al., 2001). **(B)** rXKR9 sequence comparing location of predicted (top, magenta) and actual TM helices (bottom colored as in Figure 4A). The low score in the prediction of TM3 and the high score in the region around IH2 is apparent.

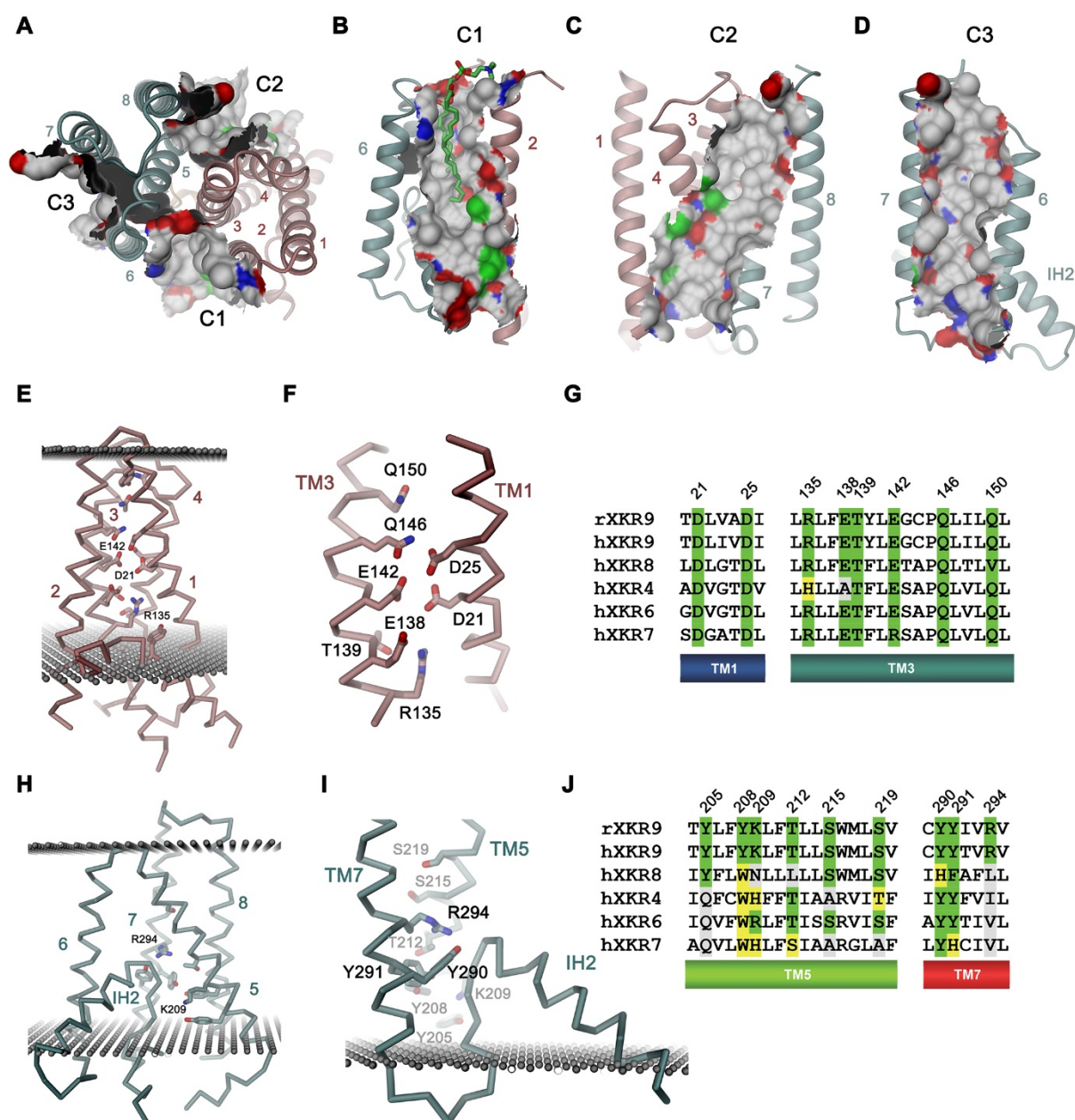


Figure 5. Features of the rXKR9 structure of potential functional relevance. (A-D) Cavities on the surface of the rXKR9 structure that are suitable for lipid interactions. Segments of the protein are displayed as ribbon. Sections of the molecular surface are shown and colored according to the contacting atoms (carbon: grey, oxygen: red, nitrogen: blue, sulfur: green). Transmembrane helices are numbered and cavities are labelled (C1-C3). (A) View from the extracellular side. (B), Cavities C1, (C), C2, and (D), C3 viewed from within the membrane. (E) Structure of polar residues buried in the ND. (F) Closeup of the membrane inserted parts of TM1 and 3 displaying the position of conserved polar and charged residues. (G) Sequence

alignment of the regions displayed in **F** in rXKR9 and selected human paralogs. **(H)** Structure of polar residues buried in the CD. **(I)** Closeup of the membrane inserted region encompassing TM5, TM7 and IH2 displaying the position of polar and charged residues. **(J)** Sequence alignment of the regions displayed in **H** in rXKR9 and selected human paralogs. **G, J**, Alignment of selected regions of rXKR9 (NCBI: NP_001012229.1) with hXKR9 (NCBI: NP_001011720.1), hXKR8 (NCBI: NP_060523.2), hXKR4 (NCBI: NP_443130.1), hXKR6 (NCBI: NP_775954.2) and hXKR7 (NCBI: NP_001011718.1). Secondary structure elements are indicated. Identical residues are highlighted in green, similar residues in yellow. **E, H, I**, Boundaries of the hydrophobic core of the bilayer are indicated as spheres. **C, E, H, I**, The protein is displayed as C α -trace with selected residues shown as sticks. Secondary structure elements and selected residues are labeled. **A-F, H, I** Coloring of the protein is as in Figure 4D, ND in red and CD in cyan.

Figure supplement 1. Surface electrostatics.

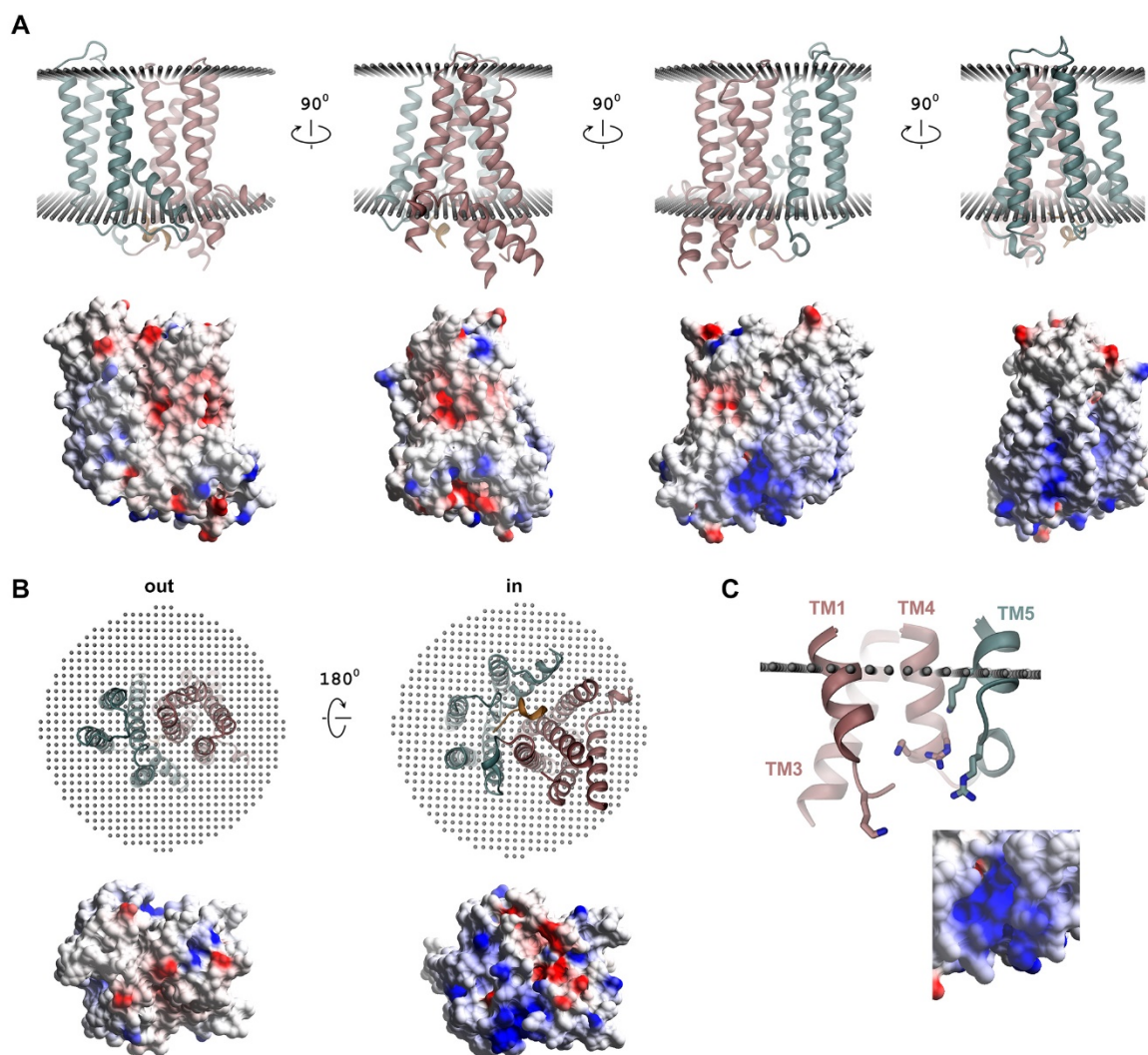


Figure 5—figure supplement 1. Surface electrostatics. **(A)** Ribbon representation of different orientations of rXKR9 viewed from within the membrane (top) and electrostatic potential mapped on the molecular surface of rXKR9 (bottom). **(B)** Ribbon representation of rXKR9 (top) and electrostatic potential mapped on the molecular surface of rXKR9 (bottom) viewed from the extracellular side (out, left) and the cytoplasm (in, right). **(C)** Section of the intracellular loops containing a cluster of positively charged residues (shown as sticks) that could provide an interaction site with negatively charged lipids with inset showing a blow-up of the electrostatic potential mapped on its surrounding surface. The view is as in **A**, third structure from the left. **A-C** Electrostatic potential calculated in Coot (Emsley and Cowtan,

2004) is mapped on the surface with the intensity of colors adjusted to its magnitude (red negative, blue positive).

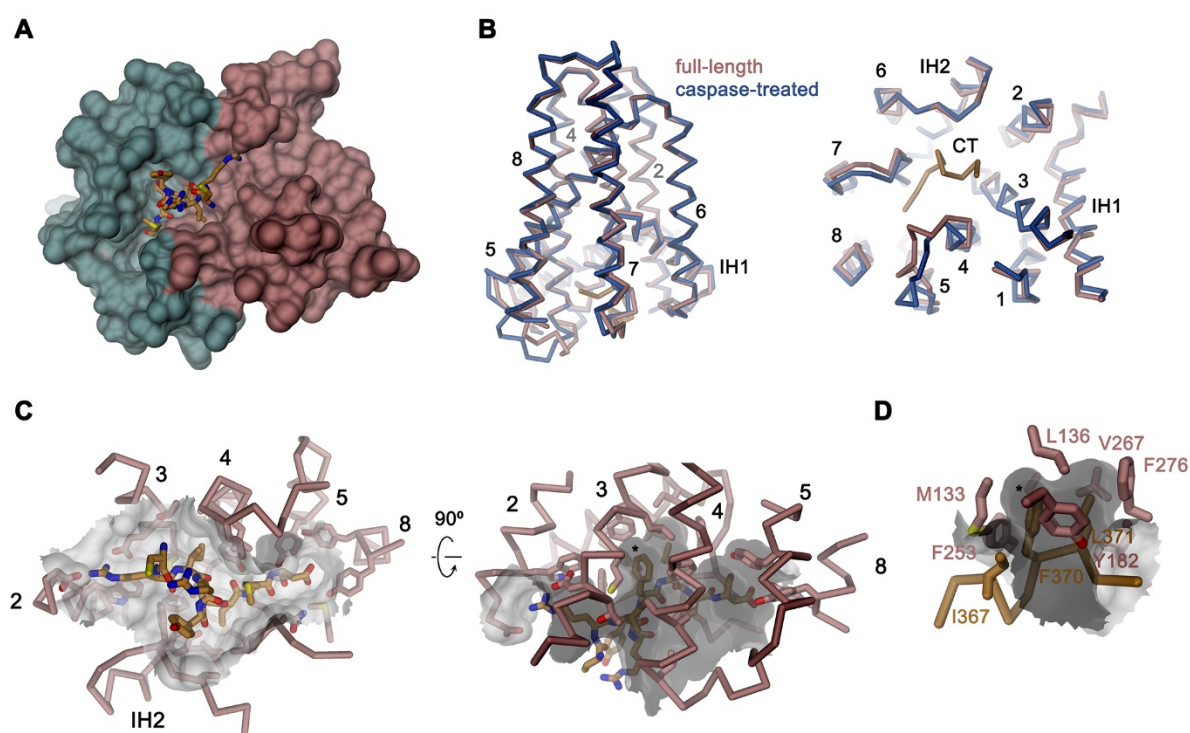


Figure 6. Binding site of the C-terminus. (A) Binding of the C-terminus of rXKR9 to a cleft of the protein. rXKR9 excluding its C-terminus is shown surface representation colored according to the two domains of the structure (as in Figure 4D). The C-terminal peptide (CT) defined in the structure is shown as stick model. (B) Superposition of the full-length and caspase-cleaved structures of rXKR9. Left, view from within the membrane. Right, view from the cytoplasm. (C) Interactions of the CT with residues lining its binding site in rXKR9. The relationship between views is indicated. (left, view from the cytoplasm, right, view from within the membrane). (D) Blowup of hydrophobic residues of the CT with its binding site. C, D, * marks position of F370. B-D, protein is shown as Ca-trace with selected residues shown as sticks.

Sections of the molecular surface are displayed. Membrane spanning helices are indicated by numbers, IH1 and IH2 and CT and selected residues are labeled explicitly.

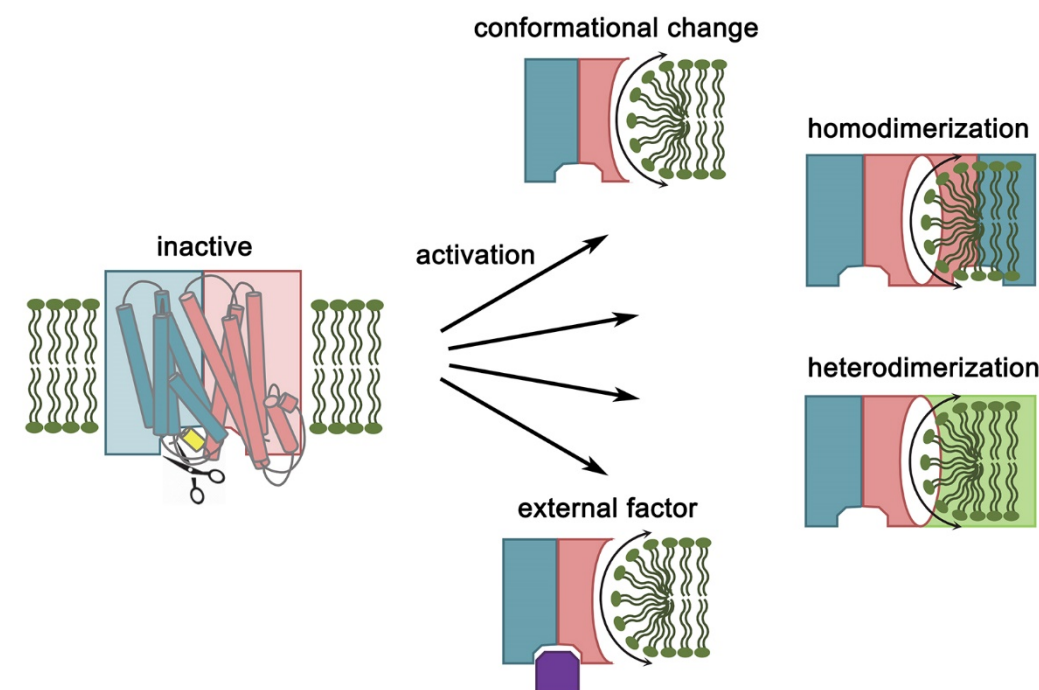


Figure 7. Schematic depiction of potential activation mechanisms. The activation of XKR9 by caspase, which releases the C-terminus interacting with the inactive protein could involve a conformational change of the protein leading to the exposure of hydrophilic residues and promote homodimerization of the protein. In an alternative scenario, the activation of the site promoting lipid transport might require interaction with another subunit. Finally, activation might require the interaction with an external factor that binds to the site released by the C-terminus or to another location that becomes accessible after caspase cleavage.

911 Table 1.

	Dataset 1 rXkr9 (EMDB-XXX) (PDB XXX)	Dataset 2 rXkr9 caspase -3 cleaved (EMDB-XXX) (PDB XXX)	Dataset 3 hXkr8+hBSG
Data collection and processing			
Microscope	FEI Titan Krios G3i	FEI Titan Krios G3i	Tecnai G ² Polara
Camera	Gatan K3 GIF	Gatan K3 GIF	Gatan K2
Magnification	130'000	130'000	130'000
Voltage (kV)	300	300	300
Electron exposure (e ⁻ /Å ²)	70	70	35
Defocus range (μm)	-1.0 to -2.4	-1.0 to -2.4	-0.8 to -2.5
Pixel size (Å)	0.651 (0.3255)	0.651 (0.3255)	1.34
Initial number of micrographs (no.)	12'396	14'929	2'212
Initial particle images (no.)	6'252'082	8'302'932	465'373
Final particle images (no.)	511'430	444'438	54'519
Symmetry imposed	C1	C1	C1
Map resolution (Å)	3.66	4.3	15.3
FSC threshold	0.143	0.143	0.143
Map resolution range (Å)	3.0 - 6.0	3.7 - 7.0	
Refinement			
Model resolution (Å)	3.77	4.3	
FSC threshold	0.5	0.5	
Map sharpening b-factor (Å ²)	-199.6	-229.9	
Model vs Map CC (mask)	0.78	0.77	
Model composition			
Non-hydrogen atoms	3662	3579	
Protein residues	453	444	
B factors (Å ²)			
Protein	53.75	67.41	
R.m.s. deviations			
Bond lengths (Å)	0.003	0.003	
Bond angles (°)	0.578	0.631	
Validation			
MolProbity score	1.79	1.82	
Clashscore	10.09	11.44	
Poor rotamers (%)	0.25	0.00	
Ramachandran plot			
Favored (%)	96.16	96.33	
Allowed (%)	3.84	3.67	
Disallowed (%)	0.00	0.00	

*Values in parentheses indicate the pixel size in super-resolution.

914 References

915 Afonine, P.V., B.K. Poon, R.J. Read, O.V. Sobolev, T.C. Terwilliger, A. Urzhumtsev, and P.D. Adams.
916 2018. Real-space refinement in PHENIX for cryo-EM and crystallography. *Acta Crystallogr D*
917 *Struct Biol.* 74:531-544.

Alvadia, C., N.K. Lim, V. Clerico Mosina, G.T. Oostergetel, R. Dutzler, and C. Paulino. 2019. Cryo-EM structures and functional characterization of the murine lipid scramblase TMEM16F. *eLife*. 8.

Balasubramanian, K., and A.J. Schroit. 2003. Aminophospholipid asymmetry: A matter of life and death. *Annu Rev Physiol*. 65:701-734.

Bers, D.M., C.W. Patton, and R. Nuccitelli. 2010. A practical guide to the preparation of Ca(2+) buffers. *Methods Cell Biol*. 99:1-26.

Bethel, N.P., and M. Grabe. 2016. Atomistic insight into lipid translocation by a TMEM16 scramblase. *Proceedings of the National Academy of Sciences of the United States of America*. 113:14049-14054.

Beyers, E.M., and P.L. Williamson. 2016. Getting to the Outer Leaflet: Physiology of Phosphatidylserine Exposure at the Plasma Membrane. *Physiol Rev*. 96:605-645.

Brunner, J.D., N.K. Lim, S. Schenck, A. Duerst, and R. Dutzler. 2014. X-ray structure of a calcium-activated TMEM16 lipid scramblase. *Nature*. 516:207-212.

Brunner, J.D., and S. Schenck. 2019. Preparation of Proteoliposomes with Purified TMEM16 Protein for Accurate Measures of Lipid Scramblase Activity. *Methods Mol Biol*. 1949:181-199.

Brunner, J.D., S. Schenck, and R. Dutzler. 2016. Structural basis for phospholipid scrambling in the TMEM16 family. *Curr Opin Struct Biol*. 39:61-70.

Bushell, S.R., A.C.W. Pike, M.E. Falzone, N.J.G. Rorsman, C.M. Ta, R.A. Corey, T.D. Newport, J.C. Christianson, L.F. Scofano, C.A. Shintre, A. Tessitore, A. Chu, Q. Wang, L. Shrestha, S.M.M. Mukhopadhyay, J.D. Love, N.A. Burgess-Brown, R. Sitsapesan, P.J. Stansfeld, J.T. Huiskonen, P. Tammaro, A. Accardi, and E.P. Carpenter. 2019. The structural basis of lipid scrambling and inactivation in the endoplasmic reticulum scramblase TMEM16K. *Nat Commun*. 10:3956.

Calenda, G., J. Peng, C.M. Redman, Q. Sha, X. Wu, and S. Lee. 2006. Identification of two new members, XPLAC and XTES, of the XK family. *Gene*. 370:6-16.

Chen, Y.Z., J. Mapes, E.S. Lee, R.R. Skeen-Gaar, and D. Xue. 2013. Caspase-mediated activation of *Caenorhabditis elegans* CED-8 promotes apoptosis and phosphatidylserine externalization. *Nat Commun*. 4:2726.

946 Emsley, P., and K. Cowtan. 2004. Coot: model-building tools for molecular graphics. *Acta Crystallogr*
947 *D Biol Crystallogr.* 60:2126-2132.

948 Falzone, M.E., and A. Accardi. 2020. Reconstitution of Proteoliposomes for Phospholipid Scrambling
949 and Nonselective Channel Assays. *Methods Mol Biol.* 2127:207-225.

950 Falzone, M.E., J. Rheinberger, B.C. Lee, T. Peyear, L. Sasset, A.M. Raczkowski, E.T. Eng, A. Di
951 Lorenzo, O.S. Andersen, C.M. Nimigean, and A. Accardi. 2019. Structural basis of Ca(2+)-
952 dependent activation and lipid transport by a TMEM16 scramblase. *eLife.* 8.

953 Geertsma, E.R., and R. Dutzler. 2011. A versatile and efficient high-throughput cloning tool for
954 structural biology. *Biochemistry.* 50:3272-3278.

955 Hutter, C.A.J., M.H. Timachi, L.M. Hürlimann, I. Zimmermann, P. Egloff, H. Göddeke, S. Kucher, S.
956 Štefanić, M. Karttunen, L.V. Schäfer, E. Bordignon, and M.A. Seeger. 2019. The extracellular
957 gate shapes the energy profile of an ABC exporter. *Nature Communications.* 10:2260.

958 Jiang, T., K. Yu, H.C. Hartzell, and E. Tajkhorshid. 2017. Lipids and ions traverse the membrane by the
959 same physical pathway in the nhTMEM16 scramblase. *eLife.* 6.

960 Kalienkova, V., V. Clerico Mosina, L. Bryner, G.T. Oostergetel, R. Dutzler, and C. Paulino. 2019.
961 Stepwise activation mechanism of the scramblase nhTMEM16 revealed by cryo-EM. *eLife.* 8.

962 Kalienkova, V., V. Clerico Mosina, and C. Paulino. 2021. The Groovy TMEM16 Family: Molecular
963 Mechanisms of Lipid Scrambling and Ion Conduction. *J Mol Biol:*166941.

964 Kobayashi, T., and A.K. Menon. 2018. Transbilayer lipid asymmetry. *Curr Biol.* 28:R386-R391.

965 Krogh, A., B. Larsson, G. von Heijne, and E.L. Sonnhammer. 2001. Predicting transmembrane protein
966 topology with a hidden Markov model: application to complete genomes. *J Mol Biol.* 305:567-
967 580.

968 Lee, B.C., G. Khelashvili, M. Falzone, A.K. Menon, H. Weinstein, and A. Accardi. 2018. Gating
969 mechanism of the extracellular entry to the lipid pathway in a TMEM16 scramblase. *Nat*
970 *Commun.* 9:3251.

971 Leventis, P.A., and S. Grinstein. 2010. The distribution and function of phosphatidylserine in cellular
972 membranes. *Annu Rev Biophys.* 39:407-427.

973 Malvezzi, M., K.K. Andra, K. Pandey, B.C. Lee, M.E. Falzone, A. Brown, R. Iqbal, A.K. Menon, and
974 A. Accardi. 2018. Out-of-the-groove transport of lipids by TMEM16 and GPCR scramblases.
975 *Proceedings of the National Academy of Sciences of the United States of America*.
976 Maruoka, M., P. Zhang, H. Mori, E. Imanishi, D.M. Packwood, H. Harada, H. Kosako, and J. Suzuki.
977 2021. Caspase cleavage releases a nuclear protein fragment that stimulates phospholipid
978 scrambling at the plasma membrane. *Mol Cell*. 81:1397-1410 e1399.
979 Menon, I., T. Huber, S. Sanyal, S. Banerjee, P. Barre, S. Canis, J.D. Warren, J. Hwa, T.P. Sakmar, and
980 A.K. Menon. 2011. Opsin is a phospholipid flippase. *Curr Biol*. 21:149-153.
981 Morra, G., A.M. Razavi, K. Pandey, H. Weinstein, A.K. Menon, and G. Khelashvili. 2018. Mechanisms
982 of Lipid Scrambling by the G Protein-Coupled Receptor Opsin. *Structure*. 26:356-367 e353.
983 Nagata, S., T. Sakuragi, and K. Segawa. 2020. Flippase and scramblase for phosphatidylserine exposure.
984 *Curr Opin Immunol*. 62:31-38.
985 Nagata, S., J. Suzuki, K. Segawa, and T. Fujii. 2016. Exposure of phosphatidylserine on the cell surface.
986 *Cell Death Differ*. 23:952-961.
987 Pettersen, E.F., T.D. Goddard, C.C. Huang, G.S. Couch, D.M. Greenblatt, E.C. Meng, and T.E. Ferrin.
988 2004. UCSF Chimera--a visualization system for exploratory research and analysis. *J Comput*
989 *Chem*. 25:1605-1612.
990 Pettersen, E.F., T.D. Goddard, C.C. Huang, E.C. Meng, G.S. Couch, T.I. Croll, J.H. Morris, and T.E.
991 Ferrin. 2021. UCSF ChimeraX: Structure visualization for researchers, educators, and
992 developers. *Protein Sci*. 30:70-82.
993 Ploier, B., and A.K. Menon. 2016. A Fluorescence-based Assay of Phospholipid Scramblase Activity.
994 *J Vis Exp*.
995 Pomorski, T., and A.K. Menon. 2006. Lipid flippases and their biological functions. *Cell Mol Life Sci*.
996 63:2908-2921.
997 Punjani, A., J.L. Rubinstein, D.J. Fleet, and M.A. Brubaker. 2017. cryoSPARC: algorithms for rapid
998 unsupervised cryo-EM structure determination. *Nature methods*. 14:290-296.
999 Punjani, A., H. Zhang, and D.J. Fleet. 2020. Non-uniform refinement: adaptive regularization improves
1000 single-particle cryo-EM reconstruction. *Nature methods*. 17:1214-1221.

1001 Rohou, A., and N. Grigorieff. 2015. CTFFIND4: Fast and accurate defocus estimation from electron
1002 micrographs. *Journal of structural biology*. 192:216-221.

1003 Rosenthal, P.B., and R. Henderson. 2003. Optimal determination of particle orientation, absolute hand,
1004 and contrast loss in single-particle electron cryomicroscopy. *J Mol Biol*. 333:721-745.

1005 Sakuragi, T., H. Kosako, and S. Nagata. 2019. Phosphorylation-mediated activation of mouse Xkr8
1006 scramblase for phosphatidylserine exposure. *Proceedings of the National Academy of Sciences
1007 of the United States of America*. 116:2907-2912.

1008 Sanner, M.F., A.J. Olson, and J.C. Spohner. 1996. Reduced surface: an efficient way to compute
1009 molecular surfaces. *Biopolymers*. 38:305-320.

1010 Sebastian, T.T., R.D. Baldrige, P. Xu, and T.R. Graham. 2012. Phospholipid flippases: building
1011 asymmetric membranes and transport vesicles. *Biochimica et biophysica acta*. 1821:1068-1077.

1012 Segawa, K., and S. Nagata. 2015. An Apoptotic 'Eat Me' Signal: Phosphatidylserine Exposure. *Trends
1013 Cell Biol*. 25:639-650.

1014 Stanfield, G.M., and H.R. Horvitz. 2000. The ced-8 gene controls the timing of programmed cell deaths
1015 in *C. elegans*. *Mol Cell*. 5:423-433.

1016 Stansfeld, P.J., J.E. Goose, M. Caffrey, E.P. Carpenter, J.L. Parker, S. Newstead, and M.S. Sansom.
1017 2015. MemProtMD: Automated Insertion of Membrane Protein Structures into Explicit Lipid
1018 Membranes. *Structure*. 23:1350-1361.

1019 Suzuki, J., D.P. Denning, E. Imanishi, H.R. Horvitz, and S. Nagata. 2013. Xk-related protein 8 and
1020 CED-8 promote phosphatidylserine exposure in apoptotic cells. *Science*. 341:403-406.

1021 Suzuki, J., E. Imanishi, and S. Nagata. 2014. Exposure of phosphatidylserine by Xk-related protein
1022 family members during apoptosis. *J Biol Chem*. 289:30257-30267.

1023 Suzuki, J., E. Imanishi, and S. Nagata. 2016. Xkr8 phospholipid scrambling complex in apoptotic
1024 phosphatidylserine exposure. *Proceedings of the National Academy of Sciences of the United
1025 States of America*. 113:9509-9514.

1026 Suzuki, J., M. Umeda, P.J. Sims, and S. Nagata. 2010. Calcium-dependent phospholipid scrambling by
1027 TMEM16F. *Nature*. 468:834-838.

1028 Tan, Y.Z., P.R. Baldwin, J.H. Davis, J.R. Williamson, C.S. Potter, B. Carragher, and D. Lyumkis. 2017.
1029 Addressing preferred specimen orientation in single-particle cryo-EM through tilting. *Nature*
1030 *methods*. 14:793-796.

1031 Whitlock, J.M., and H.C. Hartzell. 2016. Anoctamins/TMEM16 Proteins: Chloride Channels Flirting
1032 with Lipids and Extracellular Vesicles. *Annu Rev Physiol*.

1033 Zheng, S.Q., E. Palovcak, J.P. Armache, K.A. Verba, Y. Cheng, and D.A. Agard. 2017. MotionCor2:
1034 anisotropic correction of beam-induced motion for improved cryo-electron microscopy. *Nature*
1035 *methods*. 14:331-332.

1036 Zimmermann, I., P. Egloff, C.A. Hutter, F.M. Arnold, P. Stohler, N. Bocquet, M.N. Hug, S. Huber, M.
1037 Siegrist, L. Hetemann, J. Gera, S. Gmur, P. Spies, D. Gygax, E.R. Geertsma, R.J. Dawson, and
1038 M.A. Seeger. 2018. Synthetic single domain antibodies for the conformational trapping of
1039 membrane proteins. *eLife*. 7.

1040 Zimmermann, I., P. Egloff, C.A.J. Hutter, B.T. Kuhn, P. Bräuer, S. Newstead, R.J.P. Dawson, E.R.
1041 Geertsma, and M.A. Seeger. 2020. Generation of synthetic nanobodies against delicate proteins.
1042 *Nature Protocols*. 15:1707-1741.

1043 Zivanov, J., T. Nakane, B.O. Forsberg, D. Kimanius, W.J. Hagen, E. Lindahl, and S.H. Scheres. 2018.
1044 New tools for automated high-resolution cryo-EM structure determination in RELION-3. *eLife*.
1045 7.